ENERGY CATALYST
Volume 2 (2026) · ISSN 3103-9952

TECHNICAL ARTICLE

Operational-Response-Aware Two-Stage Stochastic Scheduling of Renewable Port Microgrids under Arrival-Driven Congestion and Demand Amplification

Seyed Reza Samaei[1*], K. S. Reddy[2], James Riffat[1]

[1] World Society of Sustainable Energy Technologies, Nottingham, United Kingdom
[2] Indian Institute of Technology Madras, Chennai, India

RECEIVED 28 July 2026 · REVISED 21 September 2026 · ACCEPTED 29 September 2026 · PUBLISHED 13 October 2026

ABSTRACT

Electrified container ports are coupled logistics–energy systems in which uncertain vessel arrivals determine berth occupancy, shore-power activation, cargo-handling intensity, and the residual demand balanced by renewable generation, battery storage, and the utility grid. This study develops a scenario-based stochastic framework linking a non-homogeneous vessel-arrival process to queue-consistent berth occupancy, congestion-responsive demand, photovoltaic and wind uncertainty, battery dispatch, and grid exchange. Physical arrival variability is separated from one-sided delayed Automatic Identification System (AIS) information, while a Gaussian-copula construction preserves adverse traffic–demand–renewable dependence. Five thousand stratified scenarios are reduced to 60 weighted representatives; the conditional extreme-congestion benchmark uses the nine retained Scenario-IV representatives. Across 30 independent paired out-of-sample replications, the proposed schedule reduces operating cost by 13.9% (95% Student-t CI: 13.60–14.20%), grid-import-based operational CO_2 emissions by 17.1% (16.76–17.44%), probability-weighted scenario peak grid import by 18.4% (18.03–18.77%), and cumulative operational response by 34.1% (33.50–34.70%) relative to the deterministic reference. Battery throughput is 29.4% lower than under cost-only stochastic dispatch (28.73–30.07%). In the representative seed-2026 benchmark, the corresponding in-sample reductions are 14.8%, 18.2%, 19.9%, and 36.4% relative to B0, while battery throughput is 31.6% lower than under B3. The formulation is an optimistic two-stage perfect-continuous-recourse benchmark rather than a deployable rolling-horizon controller. Within the representative synthetic system, vessel-arrival uncertainty is therefore an operational energy disturbance rather than a purely logistical input.

KEYWORDS Port microgrid, Vessel-arrival uncertainty, Shore power, Stochastic optimization, AIS uncertainty, Congestion-driven demand, Battery energy storage, Operational-response scheduling.

Abbreviations

Abbreviation	Definition
AIS	Automatic Identification System
AR(1)	First-order autoregressive process
BESS	Battery energy storage system
BOR	Berth-occupancy ratio
DE	Deterministic equivalent
ENS	Energy not served
FCFS	First-come-first-served

* Corresponding author. Email address: seyedreza.samaei1984@gmail.com (Seyed Reza Samaei)

© 2026 The Author(s).
Published by Caravel Press.

doi.org/10.65582/ec.2026.008

(continued)

Abbreviation	Definition
MIP	Mixed-integer programming
PH	Progressive hedging
PV	Photovoltaic
SOC	State of charge

1. Introduction

Ports are becoming large, actively managed electricity consumers. Shore-to-ship power, electric quay and yard equipment, refrigerated containers, terminal vehicles, buildings, and control infrastructure increasingly share the same local electrical network. At the same time, photovoltaic generation, wind generation, battery storage, and controllable grid exchange are being integrated into port energy systems. This transition can reduce local emissions and improve energy efficiency, but it changes the operational problem: electrical demand is no longer a smooth industrial profile. It responds to vessel arrivals, berth occupancy, service duration, cargo intensity, and congestion (Acciaro *et al.* 2014; Molavi *et al.* 2020; Sifakis and Tsoutsos 2021b; Buonomano *et al.* 2023).

Shore power is central to this transition because it replaces auxiliary ship generation while vessels are berthed. Its environmental value is well established, but simultaneous vessel connections can create large step changes in port demand (Sciberras *et al.* 2017; Gutierrez-Romero *et al.* 2019; Wu and Wang 2020). Research has therefore moved from stand-alone shore-power planning toward integrated berth and energy scheduling (Peng *et al.* 2021; Wang *et al.* 2022; Zhang *et al.* 2022). Renewable-assisted port microgrids extend the decision space by coordinating shore power, local generation, storage, and utility-grid interaction (Bakar *et al.* 2022; Fan *et al.* 2023). More broadly, recent research across renewable-energy and intelligent-infrastructure systems has demonstrated the complementary roles of advanced photovoltaic generation, energy storage under renewable intermittency, and digital-twin-enabled monitoring and adaptive control in improving the resilience, operational awareness, and responsiveness of electrified building, marine, and infrastructure systems (Riffat and Samaei 2025; Riffat and Samaei 2026a; Riffat and Samaei 2026c; Samaei and Riffat 2026a; Samaei and Riffat 2026b; Samaei and Riffat 2026c; Samaei and Riffat 2026d; Riffat *et al.* 2026b).

The unresolved difficulty is operational timing. Vessel arrivals are affected by weather, traffic, navigation restrictions, upstream delays, service variability, and berth congestion. Their electrical effect is discrete and event driven. A delayed vessel may reduce demand in one interval and create a concentrated shore-power and cargo-handling load later, when another vessel is already being served. Near berth saturation, a modest shift in arrival time can alter queues, service overlap, battery response, and grid ramps. Recent logistics-energy studies represent berth allocation and integrated energy operation more explicitly (Mao *et al.* 2022; Pu *et al.* 2023; Zhao *et al.* 2024; Mo *et al.* 2024; Xu *et al.* 2024). Distributionally robust, game-based, and coupled electricity-hydrogen formulations have further expanded uncertainty treatment (Ma *et al.* 2025; Sun *et al.* 2025; Li *et al.* 2025).

Recent studies have narrowed the logistics–energy gap further. Gao et al. (2025) formulated integrated port-energy scheduling under uncertain vessel-arrival information, while Lv et al. (2025) developed multistage logistics–energy scheduling with uncertain ship arrivals, cargo workload, and renewable generation. Tang et al. (2025) linked vessel schedules and handling tasks to port-load forecasting and energy dispatch. Work published in 2026 has extended the field toward day-ahead and real-time event-triggered microgrid scheduling (Li *et al.* 2026a), chance-constrained berth and onshore-power coordination under arrival and operational uncertainty (Zhao and Zhu 2026), navigational-risk-aware berth and shore-power allocation (Tang and Wang 2026), and temporally adaptive information-gap and distributionally robust logistics–energy scheduling (Xu *et al.* 2026). Robust coordination across multiple port-integrated energy systems and alternative-fuel integration

has also been examined (Li *et al.* 2026b; Saeedi *et al.* 2026). The present study therefore does not claim novelty in the general integration of uncertain vessel operations and port-energy scheduling. Its narrower contribution is the explicit separation of latent physical traffic from delayed AIS information and the quantification of how vessel-driven demand ramps propagate into controllable grid and battery responses (Figure 1).

Closer precedents include Sarantakos et al. (2024), who developed a robust joint logistics–electric framework for port power management under uncertainty in vessel arrivals, network demand, and renewable generation, and Wang et al. (2026), who integrated berth, yard, and shore-power planning under uncertain vessel-arrival times. These studies reinforce that logistics–energy integration and arrival uncertainty are established research directions. Simply augmenting the framework of Sarantakos et al. (2024) with a conventional AIS-error model would perturb the arrival information supplied to the scheduler, but it would not distinguish the latent physical vessel trajectory from the delayed observation used for commitment decisions, nor would it quantify how the resulting vessel-driven disturbance propagates separately into controllable grid and battery responses. The present framework makes both distinctions explicit by coupling a latent-physical/observed-information architecture with a response-decomposition objective and matched ex-post evaluation on the unchanged physical trajectories. The distinct contribution here is the explicit separation of latent physical traffic from delayed AIS information and the direct decomposition of vessel-driven disturbance propagation into controllable grid and battery responses.

A second issue is the distinction between physical uncertainty and information uncertainty. Vessel-arrival estimates are commonly obtained from AIS messages, which can contain timestamp delays, irregular reporting, missing messages, and erroneous manually entered fields (Harati-Mokhtari *et al.* 2007). A scheduler that treats an observed timestamp as the physical arrival state may convert a data-quality problem into a false traffic scenario. A physically delayed vessel and a correctly moving vessel whose AIS message is delayed require different operational interpretations. Recent AIS-based ETA research has moved beyond static message-quality assessments toward data-driven arrival prediction and explicit treatment of inconsistent and manually updated ETA information. Evmides et al. (2024) evaluated machine-learning ETA models using real-world AIS data, Pellemans, Slik and Bhulai (2025) showed that predictive performance varies with voyage stage and manual ETA updates, and Al Noman et al. (2025) identified data quality, transferability, uncertainty quantification, and real-time updating as continuing research challenges.

A third issue is compound uncertainty. Port demand and renewable availability are often modeled independently, although severe stress occurs when clustered arrivals coincide with photovoltaic or wind under-production. The battery must then absorb both a positive load shock and a negative generation error. A cost-only dispatch may respond through repeated charge–discharge corrections, transferring volatility from the grid to storage. Battery degradation-aware microgrid studies show that throughput and cycling materially affect operating quality (Javidsharifi *et al.* 2022; Safavi *et al.* 2025), but the link between maritime congestion and battery oscillation remains weakly represented.

Against this background, the study makes two principal conceptual contributions, supported by three methodological and validation advances:

1. A latent-physical/observed-information architecture that explicitly separates stochastic physical vessel trajectories from one-sided delayed AIS observations, so that information degradation can alter day-ahead commitment decisions without being misrepresented as a change in the underlying physical traffic.
2. An operational-response formulation that decomposes vessel-driven disturbance propagation into exogenous demand-ramp severity and controllable net-grid and battery responses, allowing the scheduler to penalize the propagation of the disturbance rather than the disturbance itself.

3. A queue-consistent arrival–occupancy–demand engine that converts stochastic physical arrivals and service durations into berth occupancy, shore-power activation, and congestion-responsive terminal demand before energy optimization.
4. A correlated scenario-generation and tail-preserving reduction procedure that retains adverse combinations of traffic, residual demand, renewable generation, and price uncertainty.
5. A two-stage stochastic mixed-integer implementation with penalty-weighted progressive-hedging coordination, feasible consensus recovery, deterministic-equivalent checking, independent out-of-sample policy evaluation, AIS robustness tests, data-scarcity experiments, sensitivity analysis, and scalability assessment.

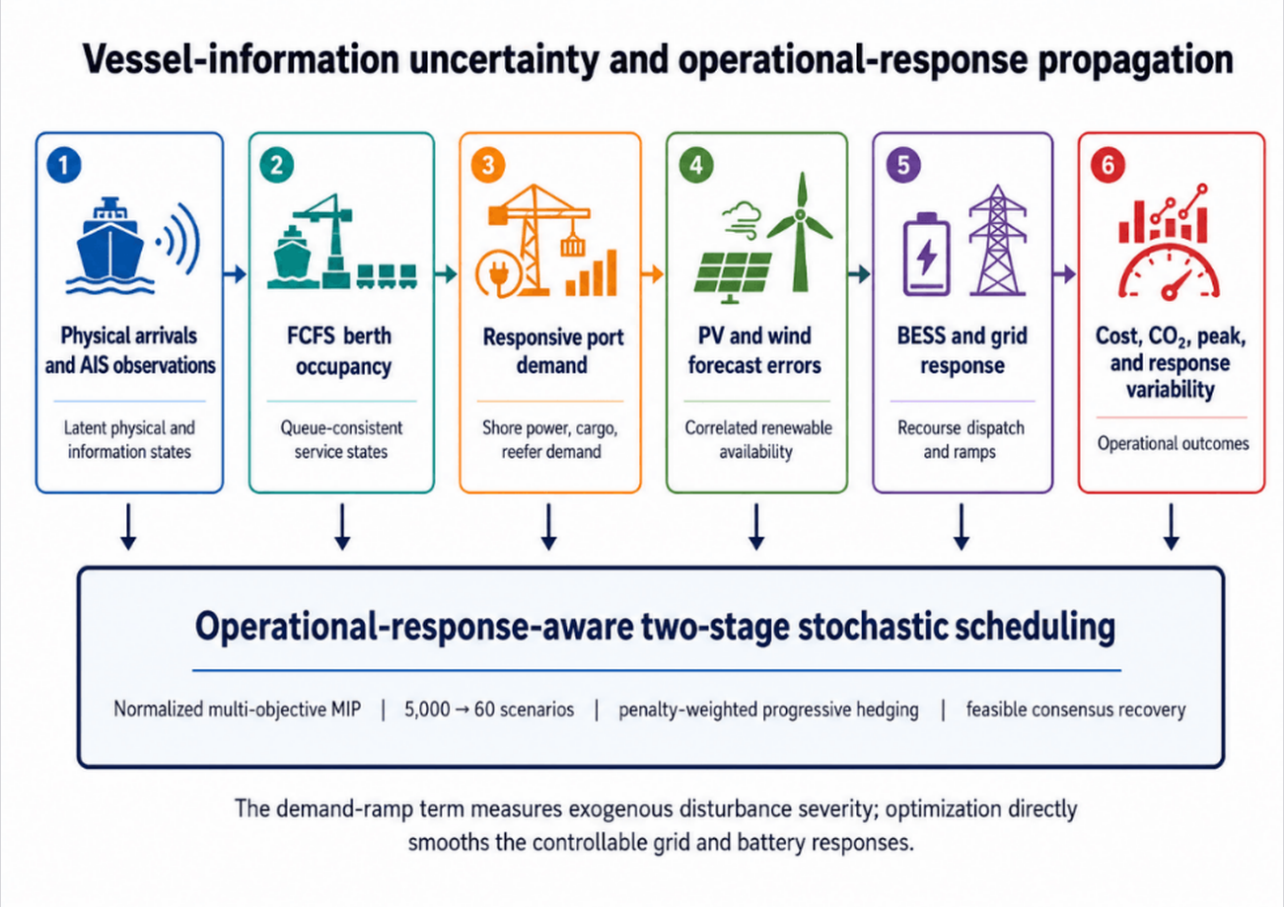

Figure 1. Propagation of vessel-arrival and information uncertainty into port demand, battery operation, and grid response within the operational-response-aware two-stage scheduling framework.

The comparison in Table 1 is limited to the formulations and performance indicators explicitly reported in the cited studies; it is not a systematic-review classification. Entries marked “not explicitly reported” indicate only that the feature was not identified in the selected formulations and do not establish absence from the wider literature. The proposed model does not co-optimize berth assignment and energy scheduling. Berth sequencing is generated by a first-come-first-served queue before optimization. Accordingly, the framework does not claim novelty from queueing, stochastic energy scheduling, or AIS-error modelling individually. Its contribution lies in the way these elements are coupled so that physical traffic and observed arrival information remain distinct and the controllable propagation of vessel-driven disturbances into grid and battery responses becomes an explicit scheduling quantity.

Table 1. Positioning of the proposed framework.

Research stream	Representative studies	Arrival and berth uncertainty	Renewable-storage coordination	Dedicated response-ramping objective explicitly reported	Remaining limitation addressed here
Shore power and port electrification	Wu and Wang (2020); Peng et al. (2021); Wang, Qi and Laporte (2022)	Partial	Limited-partial	Not explicitly reported	Event-driven demand is not linked to grid and battery response
Renewable port microgrids	Molavi et al. (2020); Sifakis, Konidakis and Tsoutsos (2021a); Bakar et al. (2022)	Limited	High	Not explicitly reported	Traffic-driven shocks remain weakly represented
Logistics-energy coordination	Mao et al. (2022); Pu et al. (2023); Zhao et al. (2024); Xu et al. (2024)	Moderate-high	Moderate-high	Not explicitly reported	Response propagation is not isolated as a scheduling target
Recent integrated uncertainty models	Gao et al. (2025); Ma et al. (2025); Lv et al. (2025); Sun et al. (2025); Li et al. (2025, 2026a, 2026b); Zhao and Zhu (2026); Tang and Wang (2026); Xu et al. (2026); Saeedi et al. (2026); Sarantakos et al. (2024); Wang et al. (2026)	High	High	Not explicitly reported	Delayed AIS information and demand–grid–battery response are not jointly isolated
Stochastic optimization and decomposition methods	Dupačová, Gröwe-Kuska and Römisch (2003); Watson and Woodruff (2011); Kaisermayer et al. (2021); Li et al. (2022)	Not port specific	High	Partial	Maritime queueing and shore-power shocks are absent
Present study	Queue-consistent stochastic port-microgrid scheduling	High, with a separate AIS layer	High	Yes	Suppresses propagation from vessel-driven demand shocks into grid and battery responses

2. System model and optimization formulation

2.1. Port operation and demand formation

The representative port contains six shore-power-equipped berths, electrically driven cargo-handling systems, refrigerated-container clusters, variable terminal services, an 18 MW photovoltaic plant, 10

MW of wind generation, a 60 MWh/20 MW battery, and a grid interconnection. The scheduling horizon contains 96 intervals of 15 min, and all power-to-energy conversions use $\Delta t = 0.25$ h.

Vessel i has physical arrival time $a_{i,s}$, service duration $T_{i,s}$, service-start time $b_{i,s}$, and departure time $d_{i,s} = b_{i,s} + T_{i,s}$ in physical scenario s. All six berths are compatible with the three modeled vessel classes. The first-come-first-served (FCFS) simulator orders vessels by physical arrival time, uses the vessel identifier as the deterministic tie-breaker, assigns the earliest-released berth, and uses berth number to resolve equal release times. The binary occupancy parameter $\delta_{i,t,s}$ equals one only while vessel i is berthed and electrically connected during interval t; waiting vessels do not activate berth-dependent demand.

The non-homogeneous Poisson process describes port-wide vessel traffic. Each port-wide arrival is routed to the modeled six-berth electrified terminal with probability $pT = 0.45$ before FCFS allocation; non-routed vessels neither enter the terminal queue nor activate its electrical demand. One 168 h warm-up realization is generated for each operating category using the same category-specific traffic, service, routing, and queueing rules as the reporting horizon. The category-specific state is held fixed across raw scenarios so that within-category differences arise after the reporting cutoff. Scenario I–IV begin with 3/0, 4/1, 5/2, and 6/5 active berths/queued vessels. The vessel-level classes, berth assignments, queue positions, residual service times, shore-power ratings, and activity states are reported in Supplementary Table S45. Five alternative warm-up seeds produce cost, peak, response, minimum-SOC, and grid-import results within one sample standard deviation of the reference initialization (Supplementary Table S46). All vessels routed before 24:00 remain in the FCFS system until service completion. The queue simulation continues for up to 30 h beyond the reporting horizon, while electrical-energy metrics remain restricted to [0, 24 h). Ramp constraints and response-index calculations begin at t = 2; no pre-horizon-to-first-interval ramp is imposed.

The berth-occupancy ratio is

$$BOR_{t,s} = \frac{1}{6}\sum_{i\in\mathcal{V}} \delta_{i,t,s} \tag{1}$$

The 15 min shore-power connection profile uses 50% of vessel-rated demand in the first and final connected intervals and 100% in fully connected intervals. Thus,

$$P_{t,s}^{SP} = \sum_{i\in\mathcal{V}} r_{i,t,s} P_i^{rated}, \qquad r_{i,t,s} \in \{0,\ 0.5,\ 1\} \tag{2}$$

The adopted hourly baseline already includes fixed building, lighting, communication, control, security, safety, and other non-responsive auxiliary demand; those loads are not added again. Congestion amplification applies only to responsive cargo handling, reefer variation, terminal transport, and variable auxiliary demand. The parameters are $BOR_{crit} = 0.85$, $n_{arr,crit} = 2$ arrivals per 15 min, $\beta B = 0.50$, $\beta A = 0.20$, and $\Gamma_{max} = 1.70$.

$$\Gamma_{t,s} = min\left\{1.70,\ \ 1 + 0.50\max\left(0,\ \frac{BOR_{t,s} - 0.85}{0.15}\right) + 0.20\min\left(1,\ \frac{N_{t,s}^{arr}}{2}\right)\right\} \tag{3}$$

The extreme-state thresholds are $BOR_{crit} = 0.85$ and $\Gamma_{crit} = 1.45$. The realized daily maximum Γ assigns the disjoint operating categories [1.00, 1.10], (1.10, 1.25], (1.25, 1.45], and (1.45, 1.70]. Total demand is

$$P_{t,s}^{D} = \left[P_t^{base} + P_{t,s}^{SP} + \Gamma_{t,s}\left(P_{t,s}^{CH} + P_{t,s}^{RF,var} + P_{t,s}^{AX,var}\right)\right]\left(1 + \varepsilon_{t,s}^{D}\right) \tag{4}$$

2.2. Renewable generation and battery storage

Available photovoltaic power is

$$P_{t,s}^{PV,av} = min\left\{18, \ \frac{\eta_{PV}\eta_{sys}A_{PV}G_{t,s}}{10^6}\right\} \tag{5}$$

with APV = 95,000 m², ηPV = 0.21, and ηsys = 0.90. At 1,000 W/m², the unrounded output is 17.955 MW and is reported as an 18 MW installed capacity. Wind speed follows a Weibull distribution with k = 2.1 and c = 8.5 m/s. Each of five 2 MW turbines produces zero below 3 m/s, follows a cubic power curve from 3 to 12 m/s, produces rated power from 12 to 25 m/s, and is shut down at or above 25 m/s.

The battery uses a single non-anticipative binary mode decision yB_t. Progressive hedging creates scenario copies $yB_{t,s}$ and coordinates them to a common recovered vector. Charge and discharge powers satisfy

$$0 \le P_{t,s}^{c} \le 20y_{t,s}^{B}, \qquad 0 \le P_{t,s}^{d} \le 20\left(1 - y_{t,s}^{B}\right) \tag{6}$$

The state-of-charge equation is

$$SOC_{t+1,s} = \left(1 - \sigma_B \Delta t\right)SOC_{t,s} + \frac{\eta_c P_{t,s}^{c}\Delta t}{E_B} - \frac{P_{t,s}^{d}\Delta t}{\eta_d E_B} \tag{7}$$

where ηc = ηd = 0.94, σB = 0.0005 h^{-1}, EB = 60 MWh, and Δt = 0.25 h. SOC is bounded between 20% and 95%, starts at 60%, and must end between 59% and 61%. Net battery power is $PB_{t,s} = Pd_{t,s} - Pc_{t,s}$ and its interval ramp is limited to 10 MW.

2.3. Grid interaction and power balance

Positive import and export are represented by continuous variables. A grid-mode binary is unnecessary because the minimum purchase price, 67.5 USD/MWh, exceeds the 45 USD/MWh export tariff; simultaneous import and export is economically dominated. Import and export are limited to 45 and 5 MW, and the net-grid ramp is limited to 10 MW per interval.

The power balance is

$$P_{t,s}^{G,imp} - P_{t,s}^{G,exp} + P_{t,s}^{PV} + P_{t,s}^{W} + P_{t,s}^{d} + P_{t,s}^{ENS} = P_{t,s}^{D} + P_{t,s}^{c} \tag{8}$$

Renewable utilization cannot exceed availability. The emergency unserved-energy variable is penalized at 10,000 USD/MWh and equals zero in all reported schedules. The remaining feasibility constraints are stated explicitly below.

$$0 \le P_{t,s}^{PV} \le P_{t,s}^{PV,av}, \qquad 0 \le P_{t,s}^{W} \le P_{t,s}^{W,av} \tag{9}$$

$$P_{t,s}^{curt} = P_{t,s}^{PV,av} + P_{t,s}^{W,av} - P_{t,s}^{PV} - P_{t,s}^{W} \ge 0 \tag{10}$$

$$0 \le P_{t,s}^{G,imp} \le 45, \quad 0 \le P_{t,s}^{G,exp} \le 5, \quad P_{t,s}^{G} = P_{t,s}^{G,imp} - P_{t,s}^{G,exp}, \quad -10 \le P_{t,s}^{G} - P_{t-1,s}^{G} \le 10 \tag{11}$$

$$P_{t,s}^{B} = P_{t,s}^{d} - P_{t,s}^{c}, \qquad -10 \le P_{t,s}^{B} - P_{t-1,s}^{B} \le 10, \qquad 0.20 \le SOC_{t,s} \le 0.95, \qquad SOC_{1,s} = 0.60, \qquad 0.59 \le SOC_{97,s} \le 0.61 \tag{12}$$

$$P_{t,s}^{ENS} \ge 0, \qquad P_{s}^{peak} \ge P_{t,s}^{G,imp} \forall\ t, \qquad P^{peak} = \sum_{s} \pi_s P_{s}^{peak} \tag{13}$$

$$u_{t,s}^{q} \ge P_{t,s}^{q} - P_{t-1,s}^{q}, \qquad u_{t,s}^{q} \ge -\left(P_{t,s}^{q} - P_{t-1,s}^{q}\right), \qquad u_{t,s}^{q} \ge 0, \qquad q \in \{D,\ G,\ B\} \tag{14}$$

2.4. Cost, emissions, peak import, and operational response

The expected operating cost is explicitly expressed in kUSD/day:

$$C_{op} = \frac{1}{1000} \sum_{s} \pi_s \sum_{t} \Delta t \left(C_{t,s}^{G} + C_{t,s}^{B} + C_{t,s}^{REN} + C_{t,s}^{curt} + C_{t,s}^{ENS}\right) \tag{15}$$

where the interval cost components are

$$C_{t,s}^{G} = \lambda_{t,s}^{buy} P_{t,s}^{G,imp} - \lambda^{sell} P_{t,s}^{G,exp}, \qquad C_{t,s}^{B} = c_B \left(P_{t,s}^{c} + P_{t,s}^{d}\right) \tag{16}$$

$$C_{t,s}^{REN} = c_{PV} P_{t,s}^{PV} + c_W P_{t,s}^{W}, \qquad C_{t,s}^{curt} = c_{curt} P_{t,s}^{curt}, \qquad C_{t,s}^{ENS} = c_{ENS} P_{t,s}^{ENS} \tag{17}$$

Grid-related operational emissions count positive grid import only:

$$E_{CO_2} = EF_G \sum_{s} \pi_s \sum_{t} P_{t,s}^{G,imp} \Delta t, \qquad EF_G = 0.47\ tCO_2/MWh \tag{18}$$

Because a constant grid-emission factor is used, the emissions result is an exact linear transformation of imported grid energy. It is retained for practical interpretation but is not treated as an independent temporal carbon-dispatch signal or as statistically independent evidence of benefit.

Operational response denotes short-horizon variability measured through demand, net-grid, and battery-power ramps. It does not denote voltage, frequency, transient, small-signal, or converter-control stability. The port microgrid is represented as a single-bus operational scheduling system; network power flow, voltage limits, harmonics, protection coordination, and sub-interval electrical dynamics are outside the formulation.

The interval response index is

$$I_{t,s} = 0.45 \frac{\left|P_{t,s}^{D} - P_{t-1,s}^{D}\right|}{10} + 0.35 \frac{\left|P_{t,s}^{G} - P_{t-1,s}^{G}\right|}{10} + 0.20 \frac{\left|P_{t,s}^{B} - P_{t-1,s}^{B}\right|}{10} \tag{19}$$

where $PG_{t,s} = PG, imp_{t,s} - PG, exp_{t,s}$ and $PB_{t,s} = Pd_{t,s} - Pc_{t,s}$; each denominator is 10 MW per 15 min. Absolute values are represented exactly with non-negative epigraph variables. For a fixed scenario set, the demand-ramp component is decision independent: it measures exogenous disturbance severity but does not alter the optimizer's minimizer. Dispatch changes induced by the response objective arise from the controllable net-grid and battery-power components. Accordingly, the proposed schedule suppresses the controllable propagation of a given vessel-driven disturbance; it does not suppress the disturbance itself.

$$I_{cum} = I^{D}_{cum} + I^{ctrl}_{cum} \tag{20}$$

$$I^{D}_{cum} = 0.45 \sum_{s} \pi_s \sum_{t=2}^{96} \frac{\left| P^{D}_{t,s} - P^{D}_{t-1,s} \right|}{10} \tag{21}$$

$$I^{ctrl}_{cum} = \sum_{s} \pi_s \sum_{t=2}^{96} \left[0.35 \frac{\left| P^{G}_{t,s} - P^{G}_{t-1,s} \right|}{10} + 0.20 \frac{\left| P^{B}_{t,s} - P^{B}_{t-1,s} \right|}{10} \right] \tag{22}$$

The expected cumulative quantity is a dimensionless interval sum:

$$I_{cum} = \sum_{s} \pi_s \sum_{t=2}^{96} I_{t,s}, \qquad I_{norm} = 100 \frac{I_{cum}}{I^{B0}_{cum}} \tag{23}$$

A scenario peak variable satisfies $\mathrm{Ppeak}_s \geq \mathrm{PG}, \mathrm{imp}_{t,s}$ for every interval, and the probability-weighted scenario peak is $\mathrm{Ppeak} = \Sigma_s \pi_s \mathrm{Ppeak}_s$. The normalized objective is

$$\min Z = 0.40 \frac{C_{op}}{121.5} + 0.20 \frac{E_{CO_2}}{321.5} + 0.30 \frac{I_{norm}}{100} + 0.10 \frac{P^{peak}}{39.2} \tag{24}$$

The four objective weights sum to one. The base value $\omega_3 = 0.30$ was selected a priori as a transparent compromise; it is not claimed to be statistically optimal, uniquely optimal, or a formally identified Pareto knee. The internal response weights 0.45/0.35/0.20 were also fixed a priori: demand remains the largest diagnostic component, while the two controllable grid and battery responses receive a combined majority weight. They are design weights rather than statistically estimated coefficients. The internal-weight sensitivity in Supplementary Table S50 illustrates the same qualitative trade-off for representative seed 2026 under equal, demand-heavy, base, and control-heavy alternatives. It is a local diagnostic and is not interpreted as a population-level robustness or significance test. The normalization references were fixed before the stochastic, robustness, and sensitivity experiments using the deterministic expected-value reference B0: 121.5 kUSD/day for operating cost, 321.5 tCO_2/day for grid-related operational emissions, 100 for cumulative response, and 39.2 MW for probability-weighted scenario peak import. These references were not retuned after observing B1–B4 or any subsequent sensitivity result; B0 therefore equals 100 by construction.

The stochastic program has a two-stage information structure. The 96 battery-mode decisions form the non-anticipative first-stage vector. Renewable utilization, curtailment, grid import and export, charge and discharge powers within the fixed mode, SOC, and emergency balancing are scenario-dependent continuous recourse. The complete daily realization is available before continuous recourse is selected. The formulation is therefore an optimistic perfect-continuous-recourse benchmark relative to sequential rolling-horizon or multistage operation and is not presented as a deployable real-time controller. Consequently,

$$y^{B}_{t,s} = y^{B}_{t,s'}, \qquad \forall\ t,\ s,\ s' \tag{25}$$

Table 2. Principal model parameters.

Component	Parameter	Value	Component	Parameter	Value
Port	Berths	6	Scheduling	Horizon / resolution	24 h / 15 min
PV	Area / efficiency / derating	95,000 m² / 21% / 0.90	PV	Installed capacity	18 MW
Wind	Turbines / total capacity	5 × 2 MW / 10 MW	Wind	Cut-in / rated / cut-out	3 / 12 / 25 m/s
BESS	Energy / power	60 MWh / 20 MW	BESS	SOC range / initial	20–95% / 60%
BESS	Charge / discharge efficiency	0.94 / 0.94	BESS	Ramp limit	10 MW/15 min
Grid	Import / export limit	45 / 5 MW	Grid	Ramp limit	10 MW/15 min
Market	Base tariffs	75 / 135 / 220 USD/MWh	Market	Stochastic purchase range	67.5–242.0 USD/MWh
Emissions	Grid factor	0.47 tCO_2/MWh	Reliability	ENS penalty	10,000 USD/MWh

Unless an external source is explicitly cited, the coefficients in Table 2 and the supplementary parameter tables are design assumptions for a representative synthetic test system rather than statistically estimated parameters for a named port. The results establish internal numerical behavior and comparative scheduling effects, not empirical prediction accuracy for a specific terminal.

3. Uncertainty modeling and solution method

3.1. Physical arrivals, service, and AIS observations

Physical arrivals follow a non-homogeneous Poisson process:

$$N_s(t+\Delta) - N_s(t) \sim Poisson\left(\int_t^{t+\Delta} \lambda_s(\tau)\, d\tau\right) \tag{26}$$

The baseline intensity is piecewise constant over six four-hour periods: 0.35, 0.55, 0.85, 0.70, 0.95, and 0.60 vessel/h, giving 16 expected port-wide arrivals/day. Category multipliers are supplemented by stochastic arrival bursts. The burst probabilities for Scenarios I–IV are 0.10, 0.20, 0.35, and 0.50; the corresponding peak caps are 0.90, 1.30, 1.80, and 2.20 vessel/h. Category-specific triangular amplitude, duration, and start-window distributions are provided in Supplementary Table S4.

Vessels are feeder, large-container, or international mega-vessel classes with probabilities 0.40, 0.45, and 0.15. Parent log-normal service-time moments are 8 ± 1.2 h, 14 ± 2.0 h, and 24 ± 3.0 h, with truncation ranges of 6–10 h, 10–18 h, and 18–30 h. The realized truncated moments are 7.910 ± 0.948 h, 13.877 ± 1.739 h, and 23.836 ± 2.616 h. Shore-power demand is uniform over 1.5–2.5 MW for feeder vessels, triangular 3/4/5 MW for large vessels, and triangular 5/6.5/8 MW for mega-vessels.

At the 00:00 day-ahead scheduling cutoff, the observed arrival estimate is

$$\hat{a}_{i,s} = a_{i,s} + \varepsilon_{i,s}^{AIS} \tag{27}$$

AIS observations are sampled at 23:00, 23:15, 23:30, 23:45, and 00:00. A single vessel–scenario delay draw is held constant across the five observations, while missingness is sampled independently at each observation time. If the 00:00 message is missing, the latest valid ETA in the preceding 60 min is

carried forward; the class-conditioned prior is used only if all five observations are missing. Across 187 vessel windows and 935 observations, the realized missing counts are 18, 47, and 93 for A1, A2, and A3, and the fallback is not invoked. The observed estimates generate forecast occupancy through the same FCFS simulator, while physical occupancy is retained for ex-post evaluation. No intra-day re-optimization is performed. For each AIS case, the observed-arrival scenario set determines the common battery-mode vector; that vector is then fixed and continuous recourse is re-solved on matched latent physical scenarios. AIS degradation therefore changes the committed mode sequence, whereas latent physical trajectories determine ex-post feasibility and performance. Physical traffic, service, renewable, price, and grid trajectories are identical across A0–A3.

A0 is error free. A1–A3 use case-specific non-negative log-normal delay distributions with log-scale parameters (μln, σln) of (1.17523, 0.93189), (2.23248, 0.71053), and (2.99589, 0.66781), producing mean/P95 delays of 5/15, 12/30, and 25/60 min. Missing-observation probabilities are 2%, 5%, and 10%, respectively. This is a one-sided delayed-arrival-information stress model, not a general unbiased ETA-error model: early ETA errors, symmetric forecasting errors, spoofing, and serially clustered communication outages are outside the experiments.

3.2. Compound scenarios and dependence

Residual-demand error is truncated normal with Scenario I–IV standard deviations of 4%, 8%, 12%, and 16% and bounds of −20% to +30%. Photovoltaic error has standard deviations of 6%, 10%, 15%, and 20% and bounds of −25% to +18%; wind error has standard deviations of 8%, 12%, 18%, and 25% and bounds of −30% to +40%. Electricity-price error is bounded at ±10%. Within-day persistence is represented by first-order autoregressive [AR(1)] processes of 0.80 for demand, 0.92 for PV, 0.95 for wind, and 0.85 for price; cargo activity and active arrival bursts use coefficients of 0.75 and 0.70.

A Gaussian copula is applied to daily scenario-level summaries ordered as [arrival, service, demand error, PV error, wind error, price error, AIS delay]^{T}. The target Spearman matrix is transformed through $R^{G}_{ij} = 2\sin(\pi\rho^{s}_{ij}/6)$, producing a positive-definite latent Gaussian matrix with minimum eigenvalue 0.312828. For interval-resolved processes, the scenario-level factor and the within-day stochastic component are generated separately. The idiosyncratic component follows a stationary standard-normal AR(1) recursion, $e_{p,t,s} = \varphi_p e_{p,t-1,s} + \sqrt{(1-\varphi_p^2)}\xi_{p,t,s}$, and the final latent process is $z_{p,t,s} = \alpha_p g_{p,s} + \sqrt{(1-\alpha_p^2)}e_{p,t,s}$. This construction preserves unit marginal variance. Service and AIS use vessel-level mappings rather than interval recursions. The calibrated α values are 0.55, 0.50, 0.60, 0.55, 0.50, 0.45, and 0.60 for arrival, service, demand, PV, wind, price, and AIS. An independent 5,000-summary validation stream gives a maximum absolute Spearman error of 0.01927 and an off-diagonal RMSE of 0.00830. A0 uses the 6 × 6 principal submatrix and fixes AIS delay at zero; A1–A3 use the full 7 × 7 matrix. The equations, calibration ranges, validation seeds, and achieved matrix are reported in Supplementary Sections S7.1 and S13.3. The calibration objective, process-specific search ranges, step sizes, and independent calibration and validation seeds are reported in Supplementary Table S8a.

3.3. Scenario reduction

Five thousand accepted joint scenarios are generated with seed 2026 using fixed category counts of 1,500, 1,750, 1,250, and 500 for Scenarios I-IV. Each raw scenario is represented by eight standardized daily scalar summaries: mean arrival intensity, mean realized service duration, maximum berth-occupancy ratio, mean total demand, total PV energy, total wind energy, mean purchase price, and an extreme-state indicator. Fast-forward probability-metric reduction is performed separately within each category using fixed retained quotas of 18, 18, 15, and 9, preserving both the aggregate category masses and the conditional extreme-congestion population. Removed mass is assigned to the nearest retained representative, so every unconditional probability is an integer multiple of 1/5,000.

Tail conditions define a priority pool rather than automatically retaining every triggered raw scenario. A raw scenario enters the pool when $\max_t \mathrm{BOR}_{t,s} \geq 0.85$, $\max_t \Gamma_{t,s} \geq 1.45$, I_s^{pre} exceeds its raw-population 95th percentile, or the category multiplier is at least 1.25 while $e_s^{\mathrm{REN}} \leq -0.20$. Candidates

are ranked by $J_s = 0.35z(BOR_s^{max}) + 0.30z(\Gamma_s^{max}) + 0.20z(I_s^{pre}) + 0.15\max(0, -z(e_s^{REN}))$. Farthest-point coverage fills the category-specific priority slots before fast-forward reduction completes the 18/18/15/9 quotas. The resulting representatives preserve category masses of 0.30, 0.35, 0.25, and 0.10. Broad-tail frequency changes from 10.8% to 10.6%; mean demand, demand variance, and the 95th percentile of peak demand are preserved within 0.7%, 2.4%, and 1.8%. The probability-metric distance is 0.036. The B4 objective is 0.775251 for 60 representatives and 0.766058 for 120 representatives, a 1.2% difference; runtime and PH iterations increase from 15.3 min and 93 iterations to 34.8 min and 117 iterations. Aggregate cluster counts appear in Supplementary Table S16, and the complete raw-ID-to-representative assignment is part of the reproducibility package.

3.4. Progressive hedging and feasible recovery

Scenario subproblems are coordinated through progressive hedging (Watson and Woodruff 2011; Kaisermayer *et al.* 2021). At iteration k, scenario s solves

$$\min_{x_s, y_s} Z_s(x_s, y_s) + \left(w_s^k\right)^{\mathsf{T}} x_s + \frac{\mu_s^k}{2} \| x_s - \bar{x}^k \|_2^2 \tag{28}$$

where x_s contains the scenario copy of the non-anticipative battery-mode vector and y_s contains scenario-dependent continuous recourse. Because binary variables and scenario-adaptive penalties are present, progressive hedging is used as a mixed-integer decomposition heuristic. The quadratic coordination term is positive semidefinite, and the continuous relaxations are convex. Since μ_s varies across scenarios, the consensus is penalty weighted rather than probability weighted alone; multipliers are updated from deviations from this weighted consensus.

$$\bar{x}^{k+1} = \frac{\sum_s \pi_s \mu_s^k x_s^{k+1}}{\sum_s \pi_s \mu_s^k}, \qquad w_s^{k+1} = w_s^k + \mu_s^k \left(x_s^{k+1} - \bar{x}^{k+1}\right) \tag{29}$$

The scenario-mean response is min–max normalized across the current scenario set, and the penalty is updated within the effective range 1–3 according to

$$\tilde{I}_s^k = \frac{\bar{I}_s^k - \min_r \bar{I}_r^k}{\max_r \bar{I}_r^k - \min_r \bar{I}_r^k + 10^{-6}}, \qquad \mu_s^{k+1} = 1 + 2\tilde{I}_s^k \in \left[1,\ 3\right] \tag{30}$$

The run-level quantities are $Z^k = \Sigma_s \pi_s Z_s(x_s^k, y_s^k)$ and $\bar{I}^k = \Sigma_s \pi_s \bar{I}_s^k$. Multipliers start at zero, penalties start at one, and the initial consensus is the deterministic expected-value B0 mode vector. Convergence requires r_x, rZ, and rI $\leq 10^{-4}$, with at most 300 iterations. Final residuals are 4.8×10^{-5}, 6.2×10^{-5}, and 7.1×10^{-5} for the full 60-scenario B4 run; conditional B1, B3, and B4 terminate in 41, 38, and 47 iterations with all residuals below tolerance. Consensus values are rounded at 0.5, exact ties use the latest feasible incumbent, and continuous recourse is re-solved after fixing the common vector. The conditional deterministic-equivalent comparison gives progressive-hedging–deterministic-equivalent (PH–DE) objective gaps of 0.229%, 0.209%, and 0.265% for B1, B3, and B4, with binary Hamming distances of 2, 1, and 2. Feasible recovery establishes feasibility under the assumed two-stage structure; the full 60-scenario run remains a heuristic decomposition without a global deterministic-equivalent certificate (Figure 2). Supplementary Tables S33 and S44 provide the run-level and validation results.

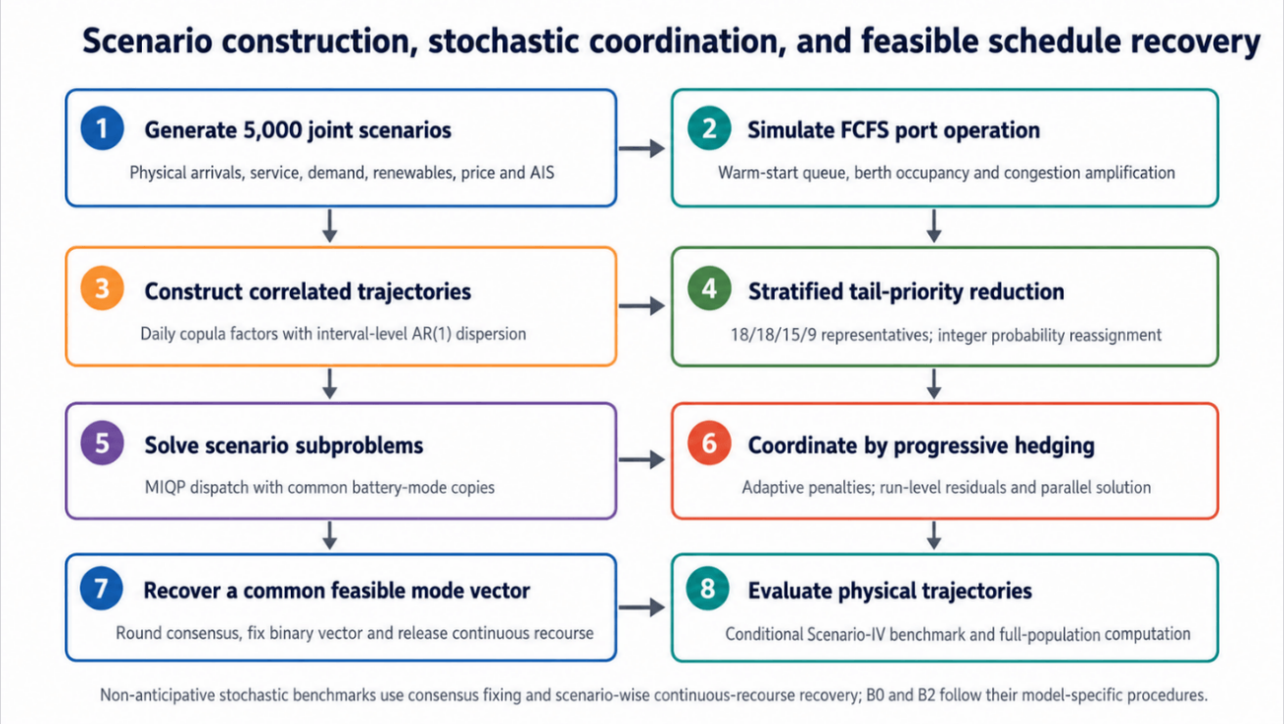

Figure 2. Joint-scenario construction, stratified tail-priority reduction, progressive-hedging coordination, and feasible consensus-recovery procedure.

The implementation uses Python 3.11.6, Pyomo 6.7.1, and Gurobi 11.0.2 on Windows 11 with an Intel Core i9-13900K processor and 64 GB RAM. Eight scenario subproblems are solved concurrently, with one Gurobi thread per worker and solver seed 2026. Each subproblem has a 0.10% relative mixed-integer-programming (MIP) gap target and a 3,600 s time limit. Reported gaps are maximum scenario-subproblem gaps at termination, not global certificates for the progressive-hedging process.

4. Case study and experimental design

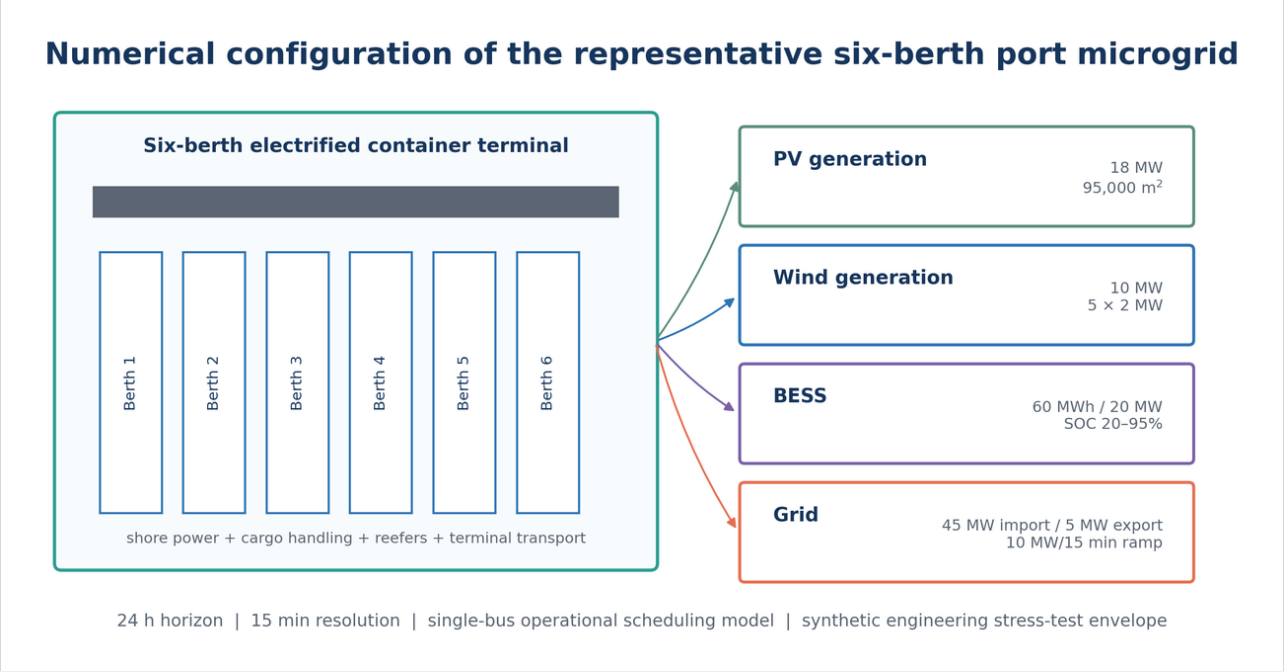

Figure 3. Numerical configuration of the representative six-berth port microgrid.

The synthetic port reproduces the demand scale and operational coupling of a medium-size electrified container terminal (Figure 3). The hourly baseline averages 8.92 MW and already contains fixed auxiliary demand. Shore power, cargo handling, reefer variation, terminal transport, and variable auxiliary demand are added according to occupancy and congestion. Under Scenario IV, total demand peaks at 41.3 MW. These inputs define a representative engineering stress-test envelope; they are not presented as a calibrated data set for a named port.

The grid purchase tariff is 75 USD/MWh from 00:00–06:00 and 22:00–24:00, 135 USD/MWh during shoulder periods, and 220 USD/MWh from 09:00–14:00 and 17:00–20:00. A ±10% deviation produces an exact range of 67.5–242.0 USD/MWh. Export receives 45 USD/MWh. PV and wind O&M costs are 4 and 8 USD/MWh, battery throughput costs 8 USD/MWh, and curtailment is penalized at 5 USD/MWh.

Table 3. Operating-scenario definitions.

Parameter	Scenario I	Scenario II	Scenario III	Scenario IV
Arrival-rate multiplier	0.80	1.00	1.25	1.50
Daily arrivals	$12 \le N < 14$	$14 \le N < 18$	$18 \le N < 22$	$22 \le N \le 26$
Peak arrival rate (vessel/h)	0.90	1.30	1.80	2.20
Service-time multiplier	0.95	1.00	1.10	1.20
Demand-error SD	4%	8%	12%	16%
PV-error SD	6%	10%	15%	20%
Wind-error SD	8%	12%	18%	25%
Congestion-factor range	[1.00, 1.10]	(1.10, 1.25]	(1.25, 1.45]	(1.45, 1.70]
Aggregate probability	0.30	0.35	0.25	0.10
Retained scenarios	18	18	15	9

After category c is drawn, a candidate scenario is generated using the corresponding arrival, service, demand, renewable, and burst parameters. If either its integer port-wide daily arrival count or its realized daily maximum congestion factor lies outside the disjoint acceptance interval in Table 3, the candidate is discarded and regenerated under the same category. Category probabilities therefore remain fixed at 0.30, 0.35, 0.25, and 0.10. The B0–B4 headline benchmark is a separate conditional extreme-congestion experiment solved using the nine retained Scenario-IV representatives, whose probabilities are renormalized within that category. It is distinct from the full 60-scenario experiment used for population characterization, scenario-reduction assessment, and computational scalability. A0 error-free AIS information is used for B0–B4; A1–A3 are evaluated in the dedicated observation-robustness experiment. B2 is deliberately information relaxed and is not interpreted as an implementable day-ahead policy.

Table 4. Benchmark definitions.

Model	Information and objective	Renewable decisions	Battery policy	Non-anticipativity and evaluation purpose
B0	Expected-value deterministic model; full four-term weights	Expected renewable profiles	Deterministic mode; continuous ex-post recourse	Expected-value reference; mode fixed and evaluated on common physical trajectories
B1	Stochastic model without response term; weights 4/7, 2/7, 0, 1/7	Scenario-dependent recourse	Non-anticipative mode with continuous recourse	Isolates the value of the explicit response penalty

Table 4. (continued)

Model	Information and objective	Renewable decisions	Battery policy	Non-anticipativity and evaluation purpose
B2	Same conventional stochastic objective as B1	Scenario-dependent recourse	Scenario-adaptive mode; non-anticipativity relaxed	Optimistic renewable-storage recourse ablation, not an implementable policy
B3	Stochastic cost-only objective; weights 1, 0, 0, 0	Scenario-dependent recourse	Non-anticipative mode with throughput cost	Conventional economically oriented battery dispatch
B4	Full objective; A0 error-free AIS information; physical arrival, service, demand, renewable, and price uncertainty	Scenario-dependent recourse	Non-anticipative mode with feasible consensus recovery	Complete proposed formulation

All models use the same initial and terminal SOC conditions, physical limits, scenario trajectories, recourse feasibility constraints, solver tolerances, and ex-post accounting (Table 4). For B0, the deterministic expected-value optimization determines the battery-mode vector; during matched ex-post evaluation, that vector is fixed while continuous grid, renewable, battery-power, SOC, curtailment, and emergency-balancing variables are re-optimized for each physical scenario under the same feasibility constraints used for B1–B4. Differences therefore arise from the listed information and objective structures rather than unequal data or tuning. All reported cross-model metrics, including peak import and operational response in formulations assigning zero objective weight to those quantities, were recomputed ex post from the recovered physical dispatch trajectories. They were not read from auxiliary peak or absolute-value epigraph variables, whose values need not be unique when the corresponding objective coefficient is zero. This post-processing rule was applied identically to B0–B4.

5. Results and discussion

5.1. Escalation from arrival uncertainty to operational response

From Scenario I to IV, average demand rises from 22.4 to 31.8 MW, a 42.0% increase (Table 5). Peak demand rises from 30.8 to 41.3 MW, while the maximum 15 min demand ramp increases from 2.4 to 9.8 MW. The berth-occupancy ratio rises from 0.51 to 0.94 and crosses the 0.85 critical threshold. The disturbance is therefore characterized not only by energy volume but also by synchronized activation near berth saturation.

Renewable penetration falls from 42.0% to 28.1% as demand grows and adverse forecast errors reduce renewable contribution. The probability-weighted mean of scenario-specific maximum battery discharge reaches 19.2 MW in Scenario IV, while the global retained-scenario maximum is 19.8 MW. The probability-weighted mean of scenario-specific minimum SOC is 24.8%, whereas the global minimum over all retained Scenario-IV scenario–state pairs is 22.6%, leaving a 2.6-percentage-point worst-case margin above the lower bound. The probability-weighted mean of scenario-specific peak grid imports under B4 is 31.4 MW, or 69.8% of the 45 MW import rating; the global import limit is enforced in every scenario.

Table 5. Operational outcomes across the four retained operating categories for representative seed 2026.

Metric	Unit	Scenario I	Scenario II	Scenario III	Scenario IV
Average port demand	MW	22.4	25.6	28.9	31.8
Probability-weighted scenario peak port demand	MW	30.8	34.7	38.6	41.3
Mean absolute demand ramp	MW/15 min	1.84	2.15	2.42	2.72
Global maximum demand ramp	MW/15 min	2.4	4.1	6.9	9.8
Probability-weighted peak berth-occupancy ratio	-	0.51	0.68	0.82	0.94
Average renewable penetration	%	42.0	38.5	33.4	28.1
Probability-weighted scenario peak grid import under B4	MW	24.6	27.9	30.2	31.4
Probability-weighted scenario maximum grid ramp	MW/15 min	3.1	4.4	5.7	6.8
Probability-weighted mean of scenario minimum SOC	%	51.8	43.6	32.4	24.8
Global minimum SOC	%	49.6	40.8	29.1	22.6
Probability-weighted mean of scenario maximum discharge power	MW	7.8	11.6	16.3	19.2
Weighted componentwise-Q95 response diagnostic	-	0.14	0.25	0.43	0.62

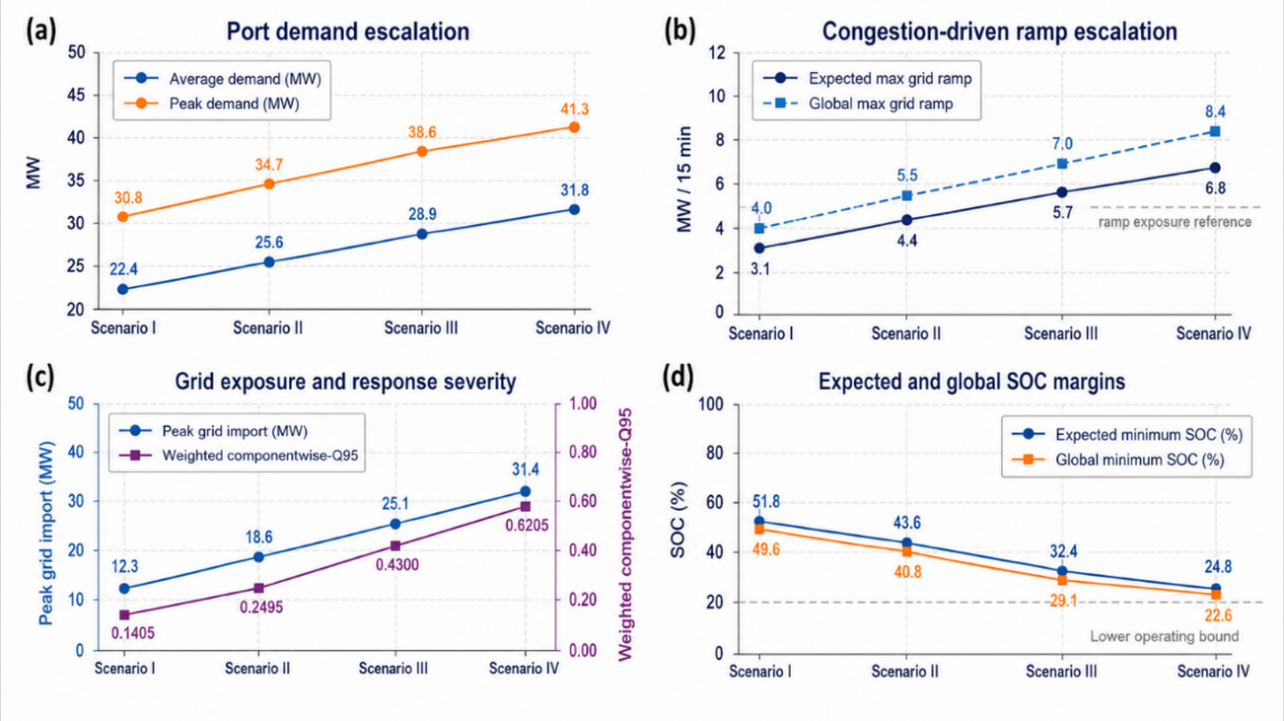

Figure 4. Escalation of port demand, congestion-driven ramps, grid exposure, expected and global SOC margins, and weighted componentwise-Q95 response severity across Scenarios I–IV for representative seed 2026.

The weighted componentwise-Q95 response diagnostic rises from 0.1405 to 0.6205, a 341.6% escalation (Figure 4). It is the weighted sum of the marginal 95th percentiles of normalized demand, net-grid, and battery ramps; it is not the 95th percentile of the combined interval response index. Component values are reported in Supplementary Table S19. Optimization benefit is assessed

through normalized cumulative response and the controllable grid and battery components across B0–B4.

5.2. Benchmark and component-ablation performance

For representative seed 2026, B4 achieves the lowest four primary metrics under the common conditional Scenario-IV evaluation (Figure 5). Daily cost falls from 121.5 to 103.5 kUSD/day, a 14.8% reduction. Grid import decreases from 684.0 to 559.6 MWh/day. At 0.47 tCO_2/MWh, this corresponds to 263.0 tCO_2/day, 18.2% below B0; emissions are therefore the linear transformation of imported grid energy. The probability-weighted scenario peak grid import falls from 39.2 to 31.4 MW, and normalized cumulative response falls from 100.0 to 63.6.

The response decomposition shows that the demand component is identical across B0–B4 because every benchmark uses the same physical demand trajectories (Table 6). In raw cumulative units, I^D remains 55.0, while B4 reduces I^G from 57.0 to 25.2 and I^B from 38.0 to 15.2. Controllable response Ictrl = $I^G + I^B$ therefore falls from 95.0 to 40.4, a 57.5% reduction. Grid and battery variability are reduced together rather than transferred from one component to the other. B2 remains an optimistic information-relaxed benchmark. B3 is cost oriented and moves 116.4 MWh/day through the battery with an 8.6 MW/15 min probability-weighted scenario maximum battery ramp; B4 lowers these values to 79.6 MWh/day and 4.9 MW/15 min. Equivalent full cycles decline from 0.97 to 0.66 cycles/day, and the 97-state pooled SOC standard deviation falls from 17.0 to 8.65 percentage points.

Energy accounting closes to numerical precision for every benchmark. Common conditional Scenario-IV demand is 763.2 MWh/day and available renewable energy is 216.844 MWh/day. Renewable-use and curtailment values for B0–B4 are 87.863/59.5%, 133.883/38.3%, 172.689/20.4%, 161.231/25.6%, and 214.459/1.1%. The high B0–B3 curtailment is associated with 398, 315, 203, and 249 positive-curtailment scenario–interval pairs, compared with 28 under B4, together with more frequent binding grid- and battery-ramp constraints. The 124.4 MWh/day grid-import reduction from B0 to B4 is explained by 126.597 MWh/day more renewable use and 27.867 MWh/day less charging, offset by 24.533 MWh/day less discharge and 5.531 MWh/day of export. Supplementary Tables S32 and S49 report the complete balance and binding-constraint decomposition.

Representative-seed component diagnostics suggest that the result is not attributable to one modeling choice. Removing cross-variable dependence raises cost, peak import, and response to 105.1 kUSD/day, 32.2 MW, and 66.7. Removing tail-priority retention increases tail-frequency error to 26.9% and response to 67.9. Replacing the adaptive PH penalty with $\mu = 1$ leaves the primary metrics nearly unchanged but increases runtime from 15.3 to 21.8 min. C6 is evaluated as a matched A3 model-misspecification test: relative to proper A3 processing, treating AIS-observed arrivals as physical raises cost by 2.3 kUSD/day, grid import by 9.5 MWh/day, scenario peak import by 0.9 MW, response by 2.7, and throughput by 4.3 MWh/day, while reducing expected minimum SOC by 0.4 percentage points. No population-level ablation significance is claimed.

Table 6. Benchmark performance and response decomposition under conditional Scenario IV.

Metric	Unit	B0	B1	B2	B3	B4
Operational cost	kUSD/day	121.5	113.8	110.4	108.8	103.5
Grid-energy import	MWh/day	684.0	637.4	597.2	609.6	559.6
Grid-related operational CO_2	tCO_2/day	321.5	299.6	280.7	286.5	263.0
Probability-weighted scenario peak grid import	MW	39.2	35.8	33.9	34.6	31.4
Normalized cumulative response	B0 = 100	100.0	84.7	78.5	74.4	63.6
Demand-response component, I^D	raw units	55.0	55.0	55.0	55.0	55.0
Grid-response component, I^G	raw units	57.0	43.8	38.0	36.2	25.2
Battery-response component, I^B	raw units	38.0	28.25	24.75	20.4	15.2
Controllable response, Ictrl	raw units	95.0	72.05	62.75	56.6	40.4

Table 6. (continued)

Metric	Unit	B0	B1	B2	B3	B4
Battery throughput	MWh/day	132.0	124.8	101.5	116.4	79.6
Equivalent full cycles	cycles/day	1.10	1.04	0.85	0.97	0.66
Mode transitions, seed 2026	transitions/day	11	10	8	10	7
Probability-weighted scenario maximum battery ramp	MW/15 min	9.2	8.9	6.2	8.6	4.9
97-state pooled SOC standard deviation	percentage points	18.2	16.3	11.8	17.0	8.65
Average grid ramp	MW/15 min	6.7	5.4	4.8	4.9	3.3
Hours above 31.36 MW	h	5.4	4.6	3.9	4.1	2.8

Note: Every absolute value in Table 6 corresponds to representative seed 2026. Cross-replication means and sample standard deviations for battery-mode transitions are reported separately in Supplementary Table S21; replicated percentage effects and their 95% confidence intervals are reported in Section 5.3 and Supplementary Table S22.

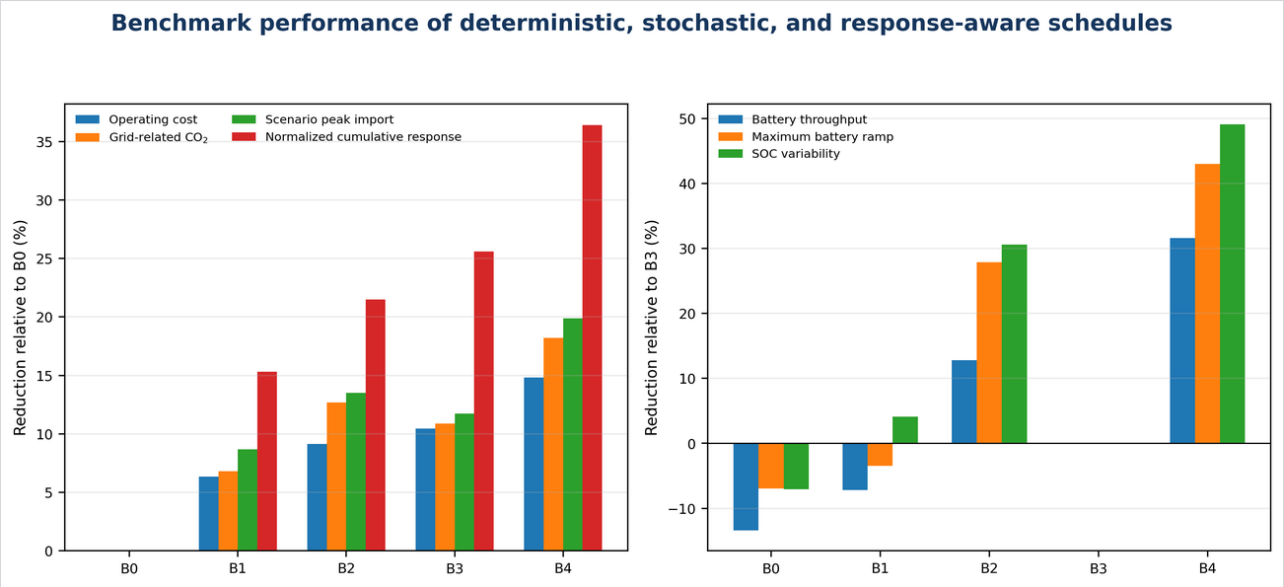

Figure 5. Relative performance of the benchmark schedules for representative seed 2026. Operating cost, grid-related CO2, probability-weighted scenario peak import, and normalized cumulative response are expressed relative to B0; battery throughput, maximum battery ramp, and SOC variability are expressed relative to B3.

The response term does not force the battery to move less in every interval. It discourages small alternating corrections with limited system value and reserves battery movement for intervals in which it reduces peak or grid-response stress.

5.3. Statistical sensitivity to the response weight

For each seed from 2026 to 2055, a new 5,000-scenario stratified training population is generated and independently reduced using the fixed 18/18/15/9 category quotas. The nine Scenario-IV representatives train the conditional first-stage battery-mode vector. Competing models use common random numbers and fixed normalization references within each seed. Percentage reductions for objective-weight sensitivity are paired before aggregation. Values are reported as mean ± sample standard deviation, with two-sided 95% Student-t confidence intervals for the replication mean, $\bar{R} \pm t_{0.975,29} sR/\sqrt{30}$. Supplementary Table S22 reports all intervals.

At $\omega_3 = 0.30$, the in-sample paired reductions are 14.8 ± 0.7% for cost, 18.2 ± 0.8% for emissions, 19.9 ± 0.9% for probability-weighted scenario peak import, 36.4 ± 1.5% for cumulative response, and 31.6 ± 1.7% for battery throughput. Their Student-t intervals are 14.54–15.06%, 17.90–18.50%, 19.56–

20.24%, 35.84–36.96%, and 30.97–32.23%. Increasing ω_3 from 0.10 to 0.50 raises response reduction from 22.6% to 38.8% but lowers cost reduction from 16.2% to 12.2%; the base weight remains a declared compromise.

Independent out-of-sample evaluation fixes each recovered first-stage vector and re-optimizes only continuous recourse on a disjoint 500-scenario Scenario-IV population using evaluation seeds 4026–4055. Across the 30 paired evaluations, B4 reduces operating cost by 13.9%, grid import and grid-related operational CO_2 by 17.1%, probability-weighted scenario peak import by 18.4%, and cumulative operational response by 34.1% relative to B0. Battery throughput is reduced by 29.4% relative to B3. Each model therefore contributes 15,000 out-of-sample scenario evaluations. All evaluations were screened for recourse feasibility, emergency unserved energy, SOC-bound compliance, grid- and battery-power compliance, terminal-SOC compliance, and numerical power-balance closure. The complete feasibility and numerical-compliance diagnostics are reported in Supplementary Table S41a; Student-t confidence intervals and seed-level reductions are reported in Table 7 and Supplementary Tables S40–S41.

Table 7. Independent out-of-sample policy evaluation across 30 paired replications.

Metric	Comparator	Mean reduction (%)	Sample SD	95% Student-t CI (%)	N
Operating cost	B4 vs B0	13.90	0.80	13.60–14.20	30
Grid import / operational CO_2	B4 vs B0	17.10	0.90	16.76–17.44	30
Probability-weighted scenario peak import	B4 vs B0	18.40	1.00	18.03–18.77	30
Cumulative operational response	B4 vs B0	34.10	1.60	33.50–34.70	30
Battery throughput	B4 vs B3	29.40	1.80	28.73–30.07	30

5.4. AIS observation robustness

AIS degradation is evaluated while holding latent physical arrivals fixed. With a 25 min mean delay, 60 min 95th-percentile delay, and 10% independently missing pre-cutoff observations, cost rises from 103.5 to 107.9 kUSD/day, the probability-weighted scenario peak grid import from 31.4 to 34.1 MW, and normalized response from 63.6 to 73.8. The probability-weighted mean of scenario-specific minimum SOC falls from 24.8% to 21.0%. The global minimum falls from 22.6% to 20.3%, leaving a 0.3-percentage-point worst-case margin above the lower bound.

Table 8. Robustness to degraded AIS observations.

Case	Mean / 95th-percentile delay (min)	Missing observations	Cost (kUSD/day)	Probability-weighted scenario peak (MW)	Response score	Expected minimum SOC (%)	Global minimum SOC (%)
A0	0 / 0 min	0%	103.5	31.4	63.6	24.8	22.6
A1	5 / 15 min	2%	104.1	31.8	64.9	24.4	22.0
A2	12 / 30 min	5%	105.3	32.6	68.1	23.3	21.2
A3	25 / 60 min	10%	107.9	34.1	73.8	21.0	20.3

The result isolates one-sided delayed information quality from physical traffic: identical latent trajectories produce a poorer day-ahead mode commitment when scenarios are built from less timely arrival information. It does not establish robustness to early ETA errors or clustered outages. A1–A3 jointly increase delay and missingness, so Table 8 reports combined effects. The representative-seed delay-by-missingness grid in Supplementary Table S38 shows monotonic descriptive effects; no

population-level factorial significance or interaction test is claimed. The matched A3–C6 comparison is reported in Supplementary Table S48.

5.5. Compound errors and synthetic fitting-history scarcity

At an arrival multiplier of 1.00, a 20% renewable shortfall raises the response score from 42.1 to 50.3. At a multiplier of 1.50, the same shortfall raises it from 55.4 to 63.6. The joint extreme case is worse than either single stressor, but the factorial contrasts do not support a positive super-additive interaction: the interaction contrasts are -0.8 kUSD/day for cost, -1.1 MW for peak import, and 0.0 for the response score. The joint case is therefore interpreted as accumulation of concurrent adverse effects rather than nonlinear synergy.

Synthetic fitting-history length affects tail representation. For each fitting length, 30 circular moving-block bootstrap samples with 7-day blocks are fitted and evaluated out of sample on a common independent 5,000-scenario reference population generated with seed 3026 (Kunsch 1989). Six-block NHPP intensities, category probabilities, burst occurrence and shape, vessel-class probabilities, truncated service distributions, demand/PV/wind/price marginals, AR coefficients, and copula correlations are re-estimated; AIS parameters and physical design inputs remain fixed. The tail event uses the fixed seed-3026 threshold: $\max_t \mathrm{BOR}_{t,s} \geq 0.85$, $\max_t \Gamma_{t,s} \geq 1.45$, or $\mathrm{I}_s^{\mathrm{pre}}$ above the reference-population 95th percentile. Signed bias btail preserves direction, while etail = |btail| reports absolute relative error:

$$b_{tail} = 100 \frac{\hat{p}_{tail} - p_{tail}^{ref}}{p_{tail}^{ref}}, \qquad e_{tail} = |b_{tail}| \tag{31}$$

Reducing the fitting sample from 365 to 30 days increases mean absolute tail-probability error from 1.2% to 10.7%, cost from 103.5 to 107.4 kUSD/day, and response from 63.6 to 69.9 (Figure 6). The 30-day block-length sensitivity gives cost/response/tail-error values of 107.0 ± 1.7, 69.2 ± 2.9, and 9.8 ± 3.4% for 3-day blocks; 107.4 ± 1.9, 69.9 ± 3.2, and 10.7 ± 3.8% for 7-day blocks; and 108.1 ± 2.3, 71.0 ± 3.7, and 12.1 ± 4.4% for 14-day blocks. Direction-specific under-representation is claimed only when the signed bias is negative.

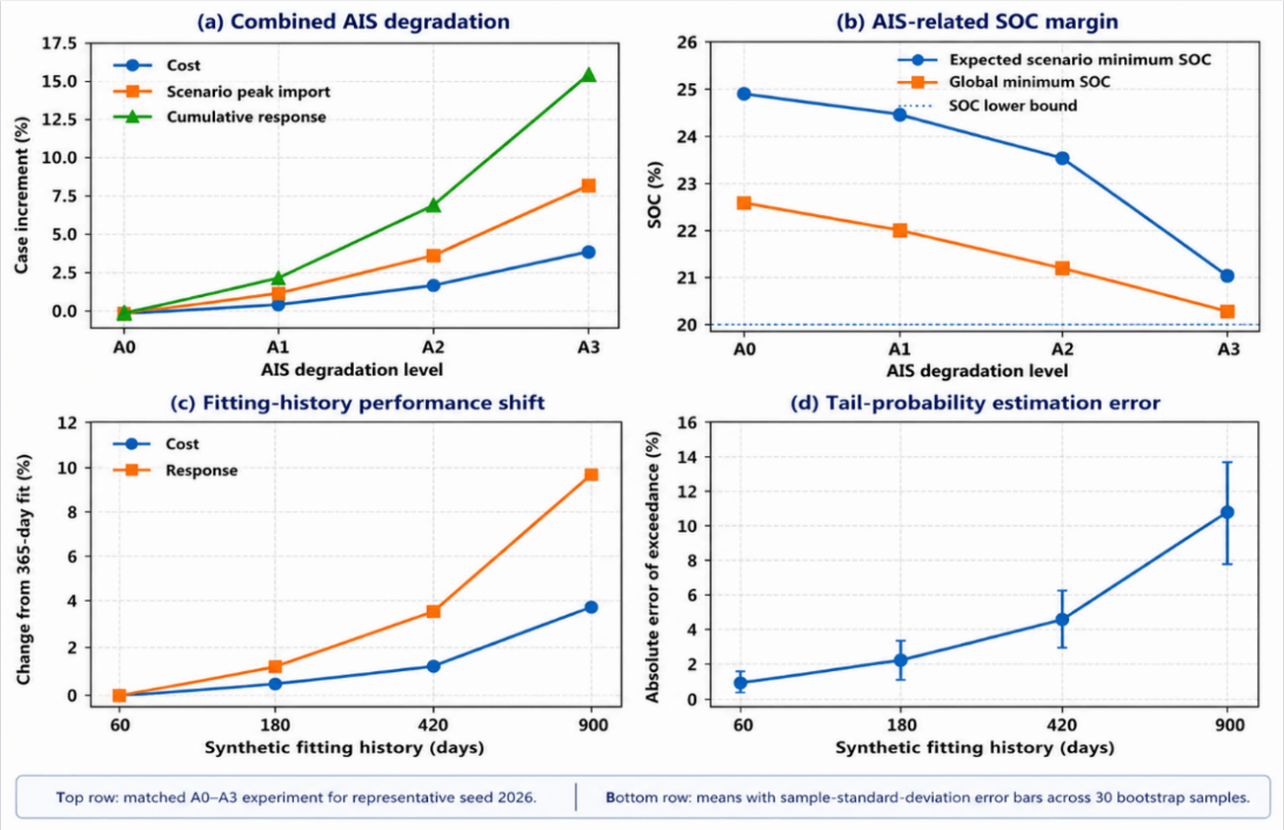

Figure 6. Robustness to delayed AIS information and synthetic fitting-history scarcity. Panels (a) and (b) report the matched A0–A3 experiment for representative seed 2026; panels (c) and (d) report means and sample-standard-deviation error bars across 30 circular moving-block bootstrap samples.

5.6. Joint BESS rating and renewable sensitivity

The BESS sensitivity scales energy and power jointly while preserving a 3 h energy-to-power ratio (Figure 7). The net-power ramp limit is scaled at 50% of converter rating per 15 min, giving limits of 5.0, 7.5, 10.0, 12.5, and 15.0 MW for the 10, 15, 20, 25, and 30 MW cases. The experiment therefore quantifies the combined BESS rating rather than the independent marginal effects of energy capacity and converter power. Increasing the rating from 30 MWh/10 MW to 60 MWh/20 MW raises cost reduction from 9.8% to 14.8% and response reduction from 22.7% to 36.4%. Increasing it to 90 MWh/30 MW improves those values only to 15.6% and 39.0%, indicating diminishing returns.

Renewable-penetration cases are generated by scaling the available PV and wind trajectories by 0.70, 1.00, 1.30, and 1.65 while holding normalized weather shapes, demand scenarios, battery limits, and grid limits unchanged. The corresponding effective PV/wind capacities are 12.6/7.0, 18.0/10.0, 23.4/13.0, and 29.7/16.5 MW. Expected penetration and curtailment rate are

$$RP = 100\frac{\sum_{s,t}\pi_s\left(P_{t,s}^{PV}+P_{t,s}^{W}\right)\Delta t}{\sum_{s,t}\pi_s P_{t,s}^{D}\Delta t} \tag{32}$$

$$CR = 100\frac{\sum_{s,t}\pi_s P_{t,s}^{curt}\Delta t}{\sum_{s,t}\pi_s\left(P_{t,s}^{PV,av}+P_{t,s}^{W,av}\right)\Delta t} \tag{33}$$

At 20% penetration, curtailment is 0.2%; at 42%, it is 7.8%. Higher penetration should therefore be accompanied by commensurate storage, flexible-load, export, or multi-energy conversion capability.

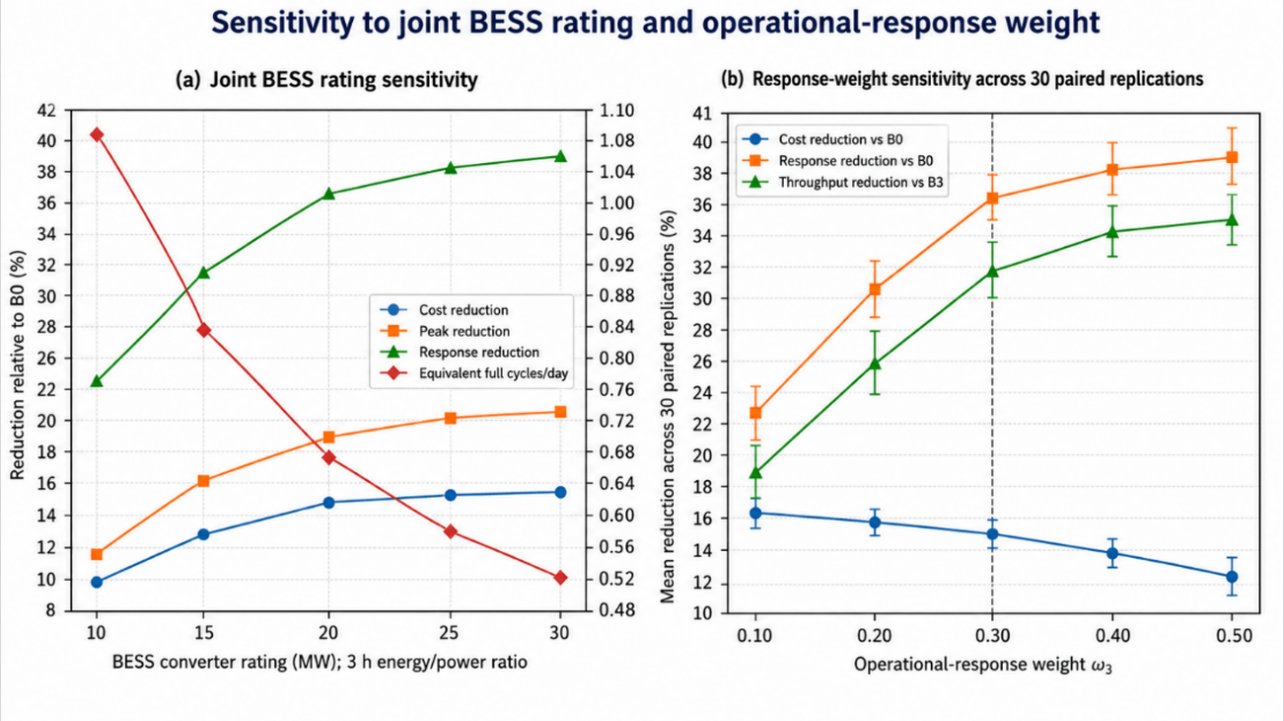

Figure 7. Sensitivity to the joint battery energy–power rating and the objective weight assigned to operational response. Panel (a) reports representative seed 2026 and expresses cost, probability-weighted scenario peak, and response reductions relative to B0. Panel (b) reports means and sample-standard-deviation error bars across 30 paired scenario-set replications; cost and response reductions are relative to B0, whereas battery-throughput reduction is relative to B3.

5.7. Computational performance

The six-berth, 60-scenario case contains 86,460 continuous variables, 5,760 battery-mode copies, and 132,420 constraints. It terminates in 93 iterations and 15.3 min after all three residuals meet 10^{-4}, with a maximum scenario-subproblem gap of 0.074%. The recovered objective is 0.775251. Increasing to 120 representatives raises runtime to 34.8 min and 117 iterations, with recovered objective 0.766058. The conditional nine-scenario deterministic-equivalent comparison gives a 0.265% PH–DE gap for B4.

The two- and four-terminal experiments replicate independent single-terminal scheduling blocks to assess computational growth. The reported constraint totals include the replicated terminal-local constraints plus 3,060 and 10,080 bookkeeping, aggregation, and consensus-accounting constraints for the two- and four-terminal cases, respectively. These additional constraints collect terminal-level objective and residual statistics; they do not impose inter-terminal power exchange, shared network power flow, or coupled berth operations. The runtimes therefore demonstrate scalability with replicated model size rather than a fully coupled multi-terminal network (Table 9).

Table 9. Computational scalability.

Configuration	Scenarios	Continuous variables	Binary variables	Constraints	PH iterations	Runtime (min)	Max. subproblem gap
1 terminal, 6 berths	30	43,230	2,880	66,210	72	6.9	0.071%
1 terminal, 6 berths	60	86,460	5,760	132,420	93	15.3	0.074%
1 terminal, 6 berths	120	172,920	11,520	264,840	117	34.8	0.081%
2 replicated terminals, 12 berths	60	173,040	11,520	267,900	121	41.6	0.089%
4 replicated terminals, 24 berths	60	346,080	23,040	539,760	158	102.4	0.097%

5.8. Practical interpretation and limitations

Three operational implications follow. First, port demand forecasts should be conditioned on vessel operations rather than treated as independent load series. Second, battery dispatch should be assessed through ramping, throughput, and SOC variability in addition to cost. Third, delayed vessel information can reduce the available SOC margin above the lower operating bound even when physical traffic is unchanged.

The study remains a numerical evaluation of a representative synthetic port. Berth assignment and sequencing are generated before energy optimization rather than co-optimized. The two-stage formulation gives continuous recourse access to the complete daily scenario after the mode sequence is committed and is therefore optimistic relative to multistage or rolling-horizon operation. The independent out-of-sample experiment reduces representative-set overfitting risk but does not remove the perfect-recourse assumption. All out-of-sample recourse problems remain feasible and use zero emergency unserved energy; however, the global minimum SOC values lie effectively on the enforced 20% lower operating bound. The out-of-sample experiment therefore demonstrates constraint feasibility but does not establish a positive reserve margin against additional forecast error, unrepresented contingencies, or model misspecification. Initial queue composition is conditioned on one category-specific warm-up realization, although five alternative warm-up seeds produce outcomes within one sample standard deviation. AIS experiments cover one-sided delay and independent pre-cutoff missing flags; early-arrival errors, symmetric ETA errors, spoofing, and clustered outages are not tested. The C0–C6 component diagnostics, AIS delay-by-missingness factorial experiment, and internal response-weight sensitivity are representative-seed analyses; no population-level statistical significance is claimed for these auxiliary experiments. The 15 min single-bus model excludes sub-interval dynamics, voltage and frequency behavior, converter controls, protection, and network constraints. The constant grid-emission factor makes emissions proportional to imported grid energy. Battery aging is represented through throughput, equivalent cycles, and SOC variability rather than electrochemical state of health. Progressive hedging is a mixed-integer heuristic; the conditional deterministic-equivalent comparison supports solution quality for the nine-scenario benchmark, but no global certificate is available for the full 60-scenario run. External validity requires site-specific AIS, terminal-operating-system, load, weather, tariff, marginal-emission, and sequential-update data.

6. Conclusions

This study formulated vessel-arrival-driven operational response as an explicit port-microgrid scheduling objective. Physical arrivals and service times produce queue-consistent berth occupancy; occupancy activates shore power and congestion-responsive demand; renewable uncertainty, battery dispatch, and grid exchange determine how the disturbance propagates through the energy system. One-sided delayed AIS information is separated from latent physical traffic, and correlated scenarios preserve adverse traffic–renewable conditions.

Across 30 independent paired out-of-sample Scenario-IV evaluations, B4 reduces operating cost, grid import and grid-related operational CO_2, probability-weighted scenario peak grid import, and cumulative operational response by 13.9%, 17.1%, 18.4%, and 34.1%, respectively, relative to B0. It reduces battery throughput by 29.4% relative to the cost-only stochastic benchmark B3. In representative seed 2026, the corresponding in-sample reductions are 14.8%, 18.2%, 19.9%, 36.4%, and 31.6%. The demand-response component remains fixed at 55.0 raw units across B0–B4, whereas B4 reduces grid and battery components from 57.0/38.0 to 25.2/15.2. The central result is therefore joint suppression of controllable grid and battery responses rather than transfer of volatility between them.

The most severe combined delayed-AIS and missingness case increases the response score by 16.0% and reduces the global minimum SOC to 20.3%. A 30-day synthetic fitting-history sample materially increases absolute tail-probability error. Energy decomposition closes every benchmark to numerical precision and, together with binding-constraint counts, shows that improved renewable absorption explains the grid-import benefit. Representative-seed diagnostics support the roles of dependence preservation, tail-priority reduction, adaptive coordination, and separation of observed AIS information from physical traffic. The conditional deterministic-equivalent comparison limits the recovered B4 objective gap to 0.265%, while the independent out-of-sample experiment provides a separate policy-validation layer. These conclusions concern short-horizon operational variability in a representative synthetic system; they are not claims about dynamic stability, unconditional performance over all traffic categories, or globally optimal multistage control.

Future work should co-optimize berth assignment and energy scheduling, introduce rolling-horizon state estimation, test symmetric ETA errors and clustered communication outages, calibrate battery degradation and network models with site data, and validate the framework with live port measurements. The reported evidence supports explicit representation of vessel-arrival uncertainty in the operational energy scheduling of highly electrified ports.

Declarations

Author contributions. Seyed Reza Samaei: Conceptualisation: Conceived the central research idea and developed the overall scientific objectives and contribution of the study. Methodology: Led the formulation of the simulation-based digital-twin framework, the operational-stress index, the coupled logistics–energy model, the rolling-horizon optimization strategy, and the statistical evaluation protocol. Software: Developed and implemented the simulation, optimization, data-processing, and numerical-audit workflows. Investigation: Conducted the computational experiments, sensitivity analyses, ablation studies, benchmark comparisons, and renewable-storage assessments. Formal Analysis: Performed the numerical, statistical, uncertainty, feasibility, and consistency analyses. Data Curation: Generated, organized, verified, and maintained the simulation inputs, replication-level outputs, audit records, and supplementary datasets. Validation: Verified the mathematical formulation, numerical balances, statistical results, and consistency of the manuscript and Supplementary Information. Visualization: Designed and prepared the figures, tables, workflow diagrams, and graphical presentation of the results. Writing – Original Draft: Prepared the initial manuscript and its technical sections. Writing – Review & Editing: Led the successive revisions and the final integration of the manuscript and Supplementary Information. Project Administration: Coordinated the research and manuscript-development process. K. S. Reddy: Methodology: Provided

senior methodological advice and broader scientific guidance during the development of the study. Validation: Critically reviewed the modelling assumptions, technical approach, interpretation of the results, and consistency of the conclusions. Writing – Review & Editing: Carefully reviewed the manuscript and provided substantive comments and recommendations that improved its scientific clarity, technical rigour, structure, and positioning within the field. Supervision: Provided senior academic advice and guidance during the refinement of the research and manuscript. James Riffat: Conceptualisation: Jointly developed the scientific framing, research direction, and principal contributions of the study. Methodology: Contributed substantially to the digital-twin architecture, operational and energy modelling, optimization framework, scenario design, and evaluation strategy. Software and Computational Verification: Contributed to the implementation strategy and the verification of the simulation and optimization workflow. Investigation and Formal Analysis: Contributed to the interpretation of the computational experiments, benchmark comparisons, sensitivity analyses, ablation results, and renewable-storage assessment. Validation: Critically verified the scientific reasoning, methodological completeness, numerical interpretation, and consistency of the reported findings. All authors discussed the results, contributed to the intellectual development of the study, reviewed the final manuscript, and approved the submitted version.

Funding. This research received no specific grant from any funding agency in the public, commercial, or not-for-profit sectors. The work was completed using the authors' existing academic and computational resources.

Conflicts of interest. The authors declare that they have no competing financial or non-financial interests that could have influenced the research, analysis, interpretation, or reporting of the findings presented in this manuscript.

Data availability. All data underlying the findings of this study were generated using the simulation and optimization framework described in the manuscript. The complete model parameterisation, stochastic-input definitions, scenario configurations, aggregated numerical results, statistical analyses, and audit tables are provided in the manuscript and Supplementary Information. The implementation code, software-environment lock file, minute-level state histories, vessel-event records, paired replication vectors, optimizer-substream outputs, final optimization populations, and solver logs are available from the corresponding author upon reasonable request. No confidential, personally identifiable, commercially restricted, or third-party proprietary data were used in this study.

Ethics. This study is based exclusively on synthetic operational data, mathematical modelling, and computational simulation. It did not involve human participants, animals, biological materials, personal data, or identifiable operational records. Ethical approval and informed consent were therefore not required.

Editorial independence. One or more authors of this paper serve as editors of this journal. To ensure editorial independence, these authors were fully recused from the handling of this manuscript. They took no part in the selection of reviewers, the peer-review process, or the editorial decision, which were managed independently by another editor with no involvement in the work.

References

Acciaro, Michele; Ghiara, Hilda; Cusano, Maria Inés (2014) 'Energy management in seaports: A new role for port authorities', *Energy Policy*, 71, pp. 4-12. Available at: https://doi.org/10.1016/j.enpol.2014.04.013

Bakar, Nur Najihah Abu; Guerrero, Josep M.; C. Vasquez, Juan; Bazmohammadi, Najmeh; Othman, Muzaidi; Rasmussen, Brian Dalby; Al-Turki, Yusuf A. (2022) 'Optimal Configuration and Sizing of Seaport Microgrids including Renewable Energy and Cold Ironing—The Port of Aalborg Case Study', *Energies*, 15(2), pp. 431. Available at: https://doi.org/10.3390/en15020431

Buonomano, Annamaria; Del Papa, Gianluca; Giuzio, Giovanni Francesco; Palombo, Adolfo; Russo, Giuseppe (2023) 'Future pathways for decarbonization and energy efficiency of ports: Modelling and optimization as sustainable energy hubs', *Journal of Cleaner Production*, 420, pp. 138389. Available at: https://doi.org/10.1016/j.jclepro.2023.138389

Dupačová, J.; Gröwe-Kuska, N.; Römisch, W. (2003) 'Scenario reduction in stochastic programming', *Mathematical Programming*, 95(3), pp. 493-511. Available at: https://doi.org/10.1007/s10107-002-0331-0

Evmides, Nicos; Aslam, Sheraz; Ramez, Tzioyntmprian T.; Michaelides, Michalis P.; Herodotou, Herodotos (2024) 'Enhancing Prediction Accuracy of Vessel Arrival Times Using Machine Learning', *Journal of Marine Science and Engineering*, 12(8), pp. 1362. Available at: https://doi.org/10.3390/jmse12081362

Fan, Songli; Ai, Qian; Xu, Guodong; Xing, Haijun; Gao, Yang (2023) 'Cooperative coordination between port microgrid and berthed ships with emission limitation and peak awareness', *Energy Reports*, 9, pp. 1657-1670. Available at: https://doi.org/10.1016/j.egyr.2023.04.225

Gao, Yinping; Yang, Linying; Wang, Miaomiao; Zhen, Lu (2025) 'Integrated energy scheduling under uncertainty for sustainable ports', *Transportation Research Part E: Logistics and Transportation Review*, 197, pp. 104033. Available at: https://doi.org/10.1016/j.tre.2025.104033

Gutierrez-Romero, José E.; Esteve-Pérez, Jerónimo; Zamora, Blas (2019) 'Implementing Onshore Power Supply from renewable energy sources for requirements of ships at berth', *Applied Energy*, 255, pp. 113883. Available at: https://doi.org/10.1016/j.apenergy.2019.113883

Harati-Mokhtari, Abbas; Wall, Alan; Brooks, Philip; Wang, Jin (2007) 'Automatic Identification System (AIS): Data Reliability and Human Error Implications', *Journal of Navigation*, 60(3), pp. 373-389. Available at: https://doi.org/10.1017/S0373463307004298

Javidsharifi, Mahshid; Pourroshanfekr Arabani, Hamoun; Kerekes, Tamas; Sera, Dezso; Spataru, Sergiu; Guerrero, Josep M. (2022) 'Effect of Battery Degradation on the Probabilistic Optimal Operation of Renewable-Based Microgrids', *Electricity*, 3(1), pp. 53-74. Available at: https://doi.org/10.3390/electricity3010005

Kaisermayer, Valentin; Muschick, Daniel; Horn, Martin; Gölles, Markus (2021) 'Progressive hedging for stochastic energy management systems', *Energy Systems*, 12(1), pp. 1-29. Available at: https://doi.org/10.1007/s12667-020-00401-z

Kunsch, Hans R. (1989) 'The Jackknife and the Bootstrap for General Stationary Observations', *The Annals of Statistics*, 17(3), pp. 1217–1241. Available at: https://doi.org/10.1214/aos/1176347265

Li, Ke; Yang, Fan; Wang, Lupan; Yan, Yi; Wang, Haiyang; Zhang, Chenghui (2022) 'A scenario-based two-stage stochastic optimization approach for multi-energy microgrids', *Applied Energy*, 322, pp. 119388. Available at: https://doi.org/10.1016/j.apenergy.2022.119388

Li, Peng; Dong, Zhixin; Ma, Kai; Yang, Hongjiu (2025) 'IGDT-based coordinated optimization for port berth-logistics-energy scheduling with electricity–hydrogen coupled transport', *Energy*, 336, pp. 138336. Available at: https://doi.org/10.1016/j.energy.2025.138336

Li, Lingling; Xia, Ziyi; Ji, Bingxiang; Zhu, Haojie (2026a) 'Microgrid energy optimal scheduling in ports incorporating the bidirectional event trigger mechanism', *Journal of Cleaner Production*, 568, pp. 148666. Available at: https://doi.org/10.1016/j.jclepro.2026.148666

Li, Peng; Chen, Ziyi; Ma, Kai; Yang, Hongjiu (2026b) 'Robust coordinated scheduling for multiple port-integrated energy systems using mobile energy storage vessels under source-load uncertainty', *Applied Energy*, 411, pp. 127645. Available at: https://doi.org/10.1016/j.apenergy.2026.127645

Lv, Wentao; Ye, Yujian; Cui, Tianxiang; Chen, Sheng; Xu, Dezhi; Yu, Wenwu; Huang, Di; Liu, Zhiyuan; Zhu, Jinda; Li, Tang; Strbac, Goran (2025) 'Sustainable electrified seaports: A coordinated energy and logistics scheduling approach for future maritime hubs', *Applied Energy*, 401, pp. 126645. Available at: https://doi.org/10.1016/j.apenergy.2025.126645

Ma, Kai; Feng, Yanpei; Yang, Jie; Cai, Yao; Yang, Bo; Guan, Xinping (2025) 'Two-stage distributionally robust optimization for port integrated energy system with berth allocation under uncertainties', *Energy*, 322, pp. 135588. Available at: https://doi.org/10.1016/j.energy.2025.135588

Mao, Anjia; Yu, Tiantian; Ding, Zhaohao; Fang, Sidun; Guo, Jinran; Sheng, Qianqian (2022) 'Optimal scheduling for seaport integrated energy system considering flexible berth allocation', *Applied Energy*, 308, pp. 118386. Available at: https://doi.org/10.1016/j.apenergy.2021.118386

Mo, Aiming; Zhang, Yan; Xiong, Yiyong; Ma, Fan; Sun, Lin (2024) 'Energy–Logistics Cooperative Optimization for a Port-Integrated Energy System', *Mathematics*, 12(12), pp. 1917. Available at: https://doi.org/10.3390/math12121917

Molavi, Anahita; Shi, Jian; Wu, Yiwei; Lim, Gino J. (2020) 'Enabling smart ports through the integration of microgrids: A two-stage stochastic programming approach', *Applied Energy*, 258, pp. 114022. Available at: https://doi.org/10.1016/j.apenergy.2019.114022

Noman, Abdullah Al; Heuermann, Aaron; Wiesner, Stefan; Thoben, Klaus-Dieter (2025) 'A Review of Vessel Time of Arrival Prediction on Waterway Networks: Current Trends, Open Issues, and Future Directions', *Computers*, 14(2), pp. 41. Available at: https://doi.org/10.3390/computers14020041

Pellemans, Mathijs; Slik, Jesper; Bhulai, Sandjai (2025) 'Estimating vessel arrival times in global supply chains', *Machine Learning with Applications*, 22, pp. 100751. Available at: https://doi.org/10.1016/j.mlwa.2025.100751

Peng, Yun; Dong, Meng; Li, Xiangda; Liu, Huakun; Wang, Wenyuan (2021) 'Cooperative optimization of shore power allocation and berth allocation: A balance between cost and environmental benefit', *Journal of Cleaner Production*, 279, pp. 123816. Available at: https://doi.org/10.1016/j.jclepro.2020.123816

Pu, Yue; Liu, Haoming; Wang, Jian; Hou, Yunhe (2023) 'Collaborative Scheduling of Port Integrated Energy and Container Logistics Considering Electric and Hydrogen-Powered Transport', *IEEE Transactions on Smart Grid*, 14(6), pp. 4345-4359. Available at: https://doi.org/10.1109/TSG.2023.3266601

Riffat, James; Samaei, Seyed Reza (2025) 'Recent Advances in Perovskite–Silicon Tandem Solar Cells: Progress, Challenges, and Pathways to Commercialisation', *Energy Catalyst*, 1(9), pp. 113-126. Available at: https://doi.org/10.61552/EC.2025.009

Riffat, James; Samaei, Seyed Reza (2026a) 'A Reliability-Based Framework for Phase Change Material Thermal Energy Storage under Renewable Intermittency: Linking Phase-Change Dynamics, Energy Availability and Load Matching', *Energy Catalyst*, 2, pp. 77-105. Available at: https://doi.org/10.65582/ec.2026.005

Riffat, James; Nazari, Kourosh; Samaei, Seyed Reza (2026b) 'AI-Driven Digital Twin Framework for Adaptive and Real-Time Structural Health Monitoring of Offshore Marine Structures', *Artificial Intelligence for Sustainable Cities*, 1(1), pp. 105-122. Available at: https://doi.org/10.65582/aifsc.2026.006

Riffat, James; Samaei, Seyed Reza (2026c) 'Thermochemical Energy Storage for Renewable Grids: A Critical Review of Materials, Reactor Architectures, and Integration Strategies', *Research and Reviews in Sustainability*, 2(1), pp. 17-37. Available at: https://doi.org/10.65582/rrs.2026.003

Saeedi, Sina; Aghamohammadloo, Hossein; Haakana, Juha; Lassila, Jukka (2026) 'Future energy management of port microgrids considering dual fuel engines and On-Shore Power Supply', *Energy Conversion and Management*, 352, pp. 121053. Available at: https://doi.org/10.1016/j.enconman.2026.121053

Safavi, Vahid; Vaniar, Arash Mohammadi; Bazmohammadi, Najmeh; Vasquez, Juan C.; Keysan, Ozan; Guerrero, Josep M. (2025) 'A battery degradation-aware energy management system for agricultural microgrids', *Journal of Energy Storage*, 108, pp. 115059. Available at: https://doi.org/10.1016/j.est.2024.115059

Samaei, Seyed Reza; Riffat, James (2026a) 'Cognitive Digital Twins for Climate-Resilient Building Energy Systems: Diagnosis-Informed Control under Extreme Thermal Stress', *Artificial Intelligence for Sustainable Cities*, 1(1), pp. 71-104. Available at: https://doi.org/10.65582/aifsc.2026.005

Samaei, Seyed Reza; Riffat, James (2026b) 'Field-Validated Digital Twin–Enabled Structural Health Monitoring for Offshore High-Pile Wharves', *Future Cities and Environment*, 12, pp. 22. Available at: https://doi.org/10.70917/fce-2026-010

Samaei, Seyed Reza; Riffat, James (2026c) 'From Optimization to Stability Preservation: A Self-Healing, Action-Bearing Digital Twin for Climate-Stressed Building Energy Systems', *Green Technology & Innovation*, 2(1), pp. 150-177. Available at: https://doi.org/10.65582/gti.2026.008

Samaei, Seyed Reza; Riffat, James (2026d) 'Health-Aware Digital Twins for Building Control under Climate Extremes: An Exposure-State Control Framework', *Research and Reviews in Sustainability*, 2(1), pp. 179-203. Available at: https://doi.org/10.65582/rrs.2026.011

Sarantakos, Ilias; Nikkhah, Saman; Peker, Meltem; Bowkett, Annabel; Sayfutdinov, Timur; Alahyari, Arman; Patsios, Charalampos; Mangan, John; Allahham, Adib; Bougioukou, Eleni; Murphy, Alan; Pazouki, Kayvan (2024) 'A robust Logistics-Electric framework for optimal power management of electrified ports under uncertain vessel arrival time', *Cleaner Logistics and Supply Chain*, 10, pp. 100144. Available at: https://doi.org/10.1016/j.clscn.2024.100144

Sciberras, Edward A.; Zahawi, Bashar; Atkinson, David J. (2017) 'Reducing shipboard emissions – Assessment of the role of electrical technologies', *Transportation Research Part D: Transport and Environment*, 51, pp. 227-239. Available at: https://doi.org/10.1016/j.trd.2016.10.026

Sifakis, Nikolaos; Konidakis, Stefanos; Tsoutsos, Theocharis (2021a) 'Hybrid renewable energy system optimum design and smart dispatch for nearly Zero Energy Ports', *Journal of Cleaner Production*, 310, pp. 127397. Available at: https://doi.org/10.1016/j.jclepro.2021.127397

Sifakis, Nikolaos; Tsoutsos, Theocharis (2021b) 'Planning zero-emissions ports through the nearly zero energy port concept', *Journal of Cleaner Production*, 286, pp. 125448. Available at: https://doi.org/10.1016/j.jclepro.2020.125448

Sun, Yantao; Guo, Yujia; Zhang, Qiang; Jia, Youwei (2025) 'Berth allocation and energy scheduling for all-electric ships in seaport microgrid: A Stackelberg game approach', *Energy*, 322, pp. 135640. Available at: https://doi.org/10.1016/j.energy.2025.135640

Tang, Ruoli; Ning, Siwen; Ren, Zongyang; Li, Xin; Zhang, Yan (2025) 'Novel Load Forecasting and Optimal Dispatching Methods Considering Demand Response for Integrated Port Energy System', *Journal of Marine Science and Engineering*, 13(3), pp. 421. Available at: https://doi.org/10.3390/jmse13030421

Tang, Xufeng; Wang, Ying (2026) 'Berth and shore power allocation under navigational risks: A survival analysis-based chance-constraint approach', *Operations Research Perspectives*, 17, pp. 100407. Available at: https://doi.org/10.1016/j.orp.2026.100407

Wang, Shuaian; Qi, Jingwen; Laporte, Gilbert (2022) 'Optimal subsidy design for shore power usage in ship berthing operations', *Naval Research Logistics (NRL)*, 69(4), pp. 566-580. Available at: https://doi.org/10.1002/nav.22029

Wang, Wensi; Yin, Tianrun; Yao, Baozhen; Song, Zhikun (2026) 'An integrated robust framework for berth, yard, and shore power planning considering vessel arrival uncertainty', *Ocean Engineering*, 358, pp. 125850. Available at: https://doi.org/10.1016/j.oceaneng.2026.125850

Watson, Jean-Paul; Woodruff, David L. (2011) 'Progressive hedging innovations for a class of stochastic mixed-integer resource allocation problems', *Computational Management Science*, 8(4), pp. 355-370. Available at: https://doi.org/10.1007/s10287-010-0125-4

Wu, Lingxiao; Wang, Shuaian (2020) 'The shore power deployment problem for maritime transportation', *Transportation Research Part E: Logistics and Transportation Review*, 135, pp. 101883. Available at: https://doi.org/10.1016/j.tre.2020.101883

Xu, Xianfeng; Li, Zhihan; Jiang, Xinchen; Huang, Xinrong; Lu, Yong; Li, Longjie (2024) 'Port berth allocation and microgrid cluster joint optimization scheduling based on master-slave game', *Journal of Cleaner Production*, 452, pp. 142220. Available at: https://doi.org/10.1016/j.jclepro.2024.142220

Xu, Yuhan; Duan, Xuxia; Liu, Zigang; Yu, Songyuan; Zhang, Yi; Fang, Fang (2026) 'A temporally adaptive IGDT-DRO framework for logistics–energy coordinated scheduling of port integrated energy systems', *Energy*, 351, pp. 140788. Available at: https://doi.org/10.1016/j.energy.2026.140788

Zhang, Yue; Liang, Chengji; Shi, Jian; Lim, Gino; Wu, Yiwei (2022) 'Optimal Port Microgrid Scheduling Incorporating Onshore Power Supply and Berth Allocation Under Uncertainty', *Applied Energy*, 313, pp. 118856. Available at: https://doi.org/10.1016/j.apenergy.2022.118856

Zhao, Wenna; Ma, Kai; Yang, Jie; Guo, Shiliang (2024) 'A risk-averse logistics-energy coordination optimization strategy for port energy system considering demand response program', *Electric Power Systems Research*, 231, pp. 110297. Available at: https://doi.org/10.1016/j.epsr.2024.110297

Zhao, Zheyin; Zhu, Jin (2026) 'Continuous-Time Scheduling of Berths and Onshore Power Supply in Cold-Chain Logistics: A Chance-Constrained Stochastic Programming Model and RL-ALNS Algorithm', *Mathematics*, 14(8), pp. 1292. Available at: https://doi.org/10.3390/math14081292

HOW TO CITE THIS ARTICLE

Samaei, S. R., Reddy, K. S. and Riffat, J. (2026). Operational-Response-Aware Two-Stage Stochastic Scheduling of Renewable Port Microgrids under Arrival-Driven Congestion and Demand Amplification. *Energy Catalyst*, 2, 169-196. https://doi.org/10.65582/ec.2026.008

COPYRIGHT AND LICENCE

© 2026 The Author(s). This is an open access article distributed under the terms of the Creative Commons Attribution (CC BY 4.0) licence, which permits unrestricted use, distribution and reproduction in any medium, provided the original work is properly cited.